



Cite this: DOI: 10.1039/c4cs00301b

Electronic structures and theoretical modelling of two-dimensional group-VIB transition metal dichalcogenides

Gui-Bin Liu,^{ab} Di Xiao,^c Yugui Yao,^a Xiaodong Xu^{de} and Wang Yao^{*b}

Atomically thin group-VIB transition metal dichalcogenides (TMDs) have recently emerged as a new class of two-dimensional (2D) semiconductors with extraordinary properties including the direct band gap in the visible frequency range, the pronounced spin-orbit coupling, the ultra-strong Coulomb interaction, and the rich physics associated with the valley degree of freedom. These 2D TMDs exhibit great potential for device applications and have attracted vast interest for the exploration of new physics. 2D TMDs have complex electronic structures which underlie their physical properties. Here we review the bulk electronic structures of these new 2D materials as well as the theoretical models developed at different levels, along which we sort out the understanding of the origins of a variety of properties observed or predicted.

Received 11th September 2014

DOI: 10.1039/c4cs00301b

www.rsc.org/csr

1 Introduction

Atomically thin two-dimensional (2D) forms of layered transition metal dichalcogenides (TMDs) have recently attracted remarkable

scientific and technological interest.^{1–4} These TMDs have the chemical composition of MX_2 , where M stands for the transition metal elements and X for the chalcogen elements. They exhibit a wide range of material properties, for example, NbS_2 , NbSe_2 , TaS_2 , TaSe_2 , $\beta\text{-MoTe}_2$, and Td-WTe_2 are metals in bulk form,^{5–8} while ReS_2 , ZrS_2 , MoS_2 , WS_2 , MoSe_2 , WSe_2 , and $\alpha\text{-MoTe}_2$ are semiconductors.^{2,5,6,9,10} Their layered bulk structure is the stacking of monolayers by weak van der Waals-like forces, and the realization of the 2D forms is promised by the in-plane stability of monolayers provided by the strong covalent bonds. Among the various TMDs, the group-VIB ones (M = Mo, W; X = S, Se) have been most extensively studied in 2D forms, where both the

^a School of Physics, Beijing Institute of Technology, Beijing 100081, China

^b Department of Physics and Center of Theoretical and Computational Physics, The University of Hong Kong, Hong Kong, China. E-mail: wangyao@hku.hk

^c Department of Physics, Carnegie Mellon University, Pittsburgh, Pennsylvania 15213, USA

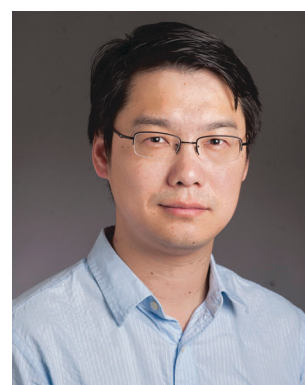
^d Department of Physics, University of Washington, Seattle, Washington, USA

^e Department of Material Science and Engineering, University of Washington, Seattle, Washington, USA



Gui-Bin Liu

research interests focus on the electronic structures and physical properties of two-dimensional materials, especially the ones related to valleytronics and spintronics.



Di Xiao

Di Xiao received his PhD in condensed matter physics from University of Texas at Austin in 2007. After working at Oak Ridge National Lab, first as a postdoctoral researcher, then a staff member, he became an Assistant Professor of Physics at Carnegie Mellon University in 2012. He is currently interested in Berry phase effects and topological phenomena in condensed matter, and applying these ideas to valley pseudospin physics in two-dimensional materials.

monolayers and few-layers are proved to be stable in air at room temperature.⁴ Each monolayer is an X–M–X covalently bonded hexagonal quasi-2D lattice (*cf.* Fig. 1), similar to graphene. Atomically thin group-VIB TMDs (monolayers, bilayers, *etc.*) have been prepared in a number of ways, including mechanical exfoliation from bulk crystals,^{1,11–13} chemical vapor deposition,^{14–17} and molecular beam epitaxy.^{18,19} Group-VIB TMDs are attracting great interest as a new class of semiconductors in the 2D limit, having remarkable electronic and optical properties.^{20,21}

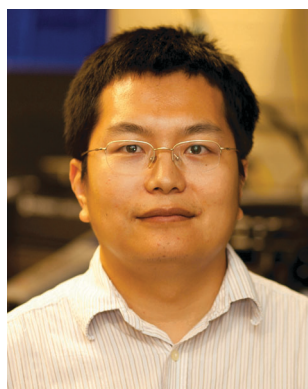
A number of extraordinary properties associated with the unique quantum degrees of freedom of electrons have been discovered in 2D group-VIB TMDs.²¹ The conduction and valence bands have degenerate extrema (*i.e.* valleys) located at the K and $-K$ points of the hexagonal Brillouin zone (BZ) (*cf.* Fig. 1c). In particular, monolayers are found to have a direct band gap at these $\pm K$ valleys,^{11,12} where the optical transitions have a valley dependent selection rule:



Yugui Yao

Yugui Yao obtained his PhD degree from Institute of Mechanics, Chinese Academy of Sciences (1999). He worked as a postdoctoral researcher successively in Institute of Physics, Chinese Academy of Sciences (IPCAS) and University of Texas at Austin (1999–2003). Then he worked successively as an assistant researcher, a research associate professor and then a research full professor in IPCAS (2001–2011). He is now a professor of School of Physics, Beij-

ing Institute of Technology. His research interests cover many fields in computational physics & condensed matter theory including first-principles calculations, Berry phase related physics, anomalous transport, 2D materials, topological insulators, and so on.



Xiaodong Xu

Xiaodong Xu has been an Assistant Professor in the Department of Physics and the Department of Materials Science and Engineering at the University of Washington since 2010. He received his PhD (Physics, 2008) from the University of Michigan and then performed postdoctoral research (2009–2010) at the Center for Nanoscale Systems at Cornell University. His current interest is in the investigation of novel electronic and optical phenomena in 2D quantum materials.

interband transitions at K ($-K$) valley couple exclusively to the right- (left-) circularly polarized light.^{22,23} This optical selection rule makes possible quantum control of the valley pseudospin, including the demonstrated optical generation and detection of valley polarization^{24–26} and valley coherence.²⁷ Moreover, the valley pseudospin is associated with the valley Hall effect that makes possible its electric control,^{23,28,29} and the valley magnetic moment for possible magnetic control.^{28,30–32} Similar to spin, these valley phenomena allow the potential use of valley pseudospin for information processing. In bilayers, electrically tunable properties of the valley pseudospin and the strong interplay between the valley pseudospin with the real spin and the layer pseudospin have also been discovered.^{33–35} 2D group-VIB TMDs could provide the platform to explore these various quantum degrees of freedom of the electrons for future electronic devices with versatile functionalities.

Because of the direct band gap in the visible frequency range, monolayer group-VIB TMDs are ideal systems to explore optoelectronic phenomena and applications in the truly 2D limit. The elementary excitation key to many optoelectronic phenomena is the exciton, a hydrogen-like bound state formed by a pair of electron and hole. Under finite doping, this neutral excitation can bind an extra electron or hole to form a charged exciton, and such a three-particle bound state is also known as a trion. Recent experiments show that excitonic physics can be remarkably interesting in 2D group-VIB TMDs. Photoluminescence (PL) measurements have demonstrated the continuous evolution from positively charged, to neutral, and then to negatively charged excitons as a function of doping controlled by gate.^{27,36,37} First-principles calculations have shown the exotic nature of excitons in 2D group-VIB TMDs: a strong binding energy of hundreds of meV, and a wave function largely of the Wannier type (*i.e.* extended over a large number of unit cells).^{38,39} The calculated binding energy agrees in orders of magnitude with recent experiments based on optical reflection spectra,⁴⁰ two-photon absorption spectra,^{41–44} and scanning



Wang Yao

Wang Yao is an Associate Professor in the Department of Physics at The University of Hong Kong. He received PhD in Physics from University of California, San Diego, in 2006, and then worked as postdoc in University of Texas at Austin. In 2008, he joined University of Hong Kong as an Assistant Professor. His research interests are quantum spintronics, and valley and spin physics in 2D materials and their heterostructures. He has received the 2013 Croucher Innovation Award, and the 2014 OCPA Achievement in Asia Award (Robert T. Poe Prize).

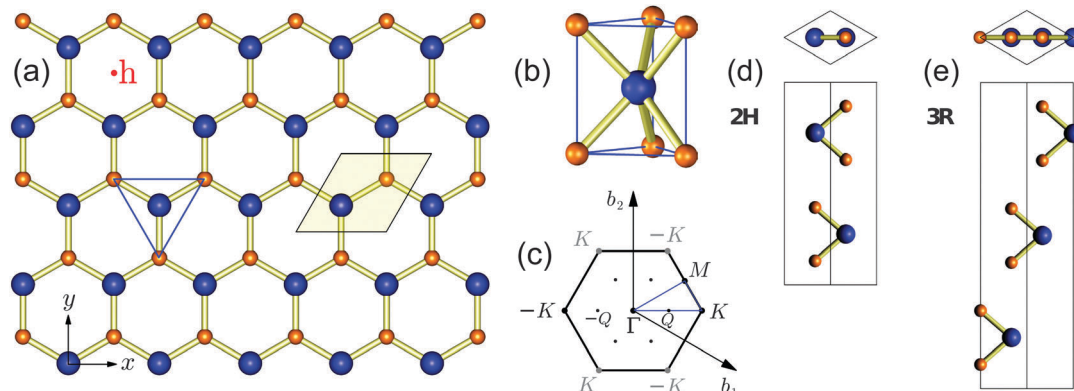


Fig. 1 (a) Top view of group-VIB TMD monolayers. The blue and orange spheres represent M and X atoms respectively. The light yellow diamond region is the 2D unit cell with lattice constant a . (b) Trigonal prismatic coordination geometry, corresponding to the blue triangle in top view. (c) The first Brillouin zone. \mathbf{b}_1 and \mathbf{b}_2 are the reciprocal lattice vectors. (d) Top and side views of the unit cell of bulk or bilayer of 2H stacking. (e) Unit cell of bulk group-VIB TMDs of 3R stacking.

tunneling microscopy and spectroscopy.^{45,46} The exceptionally large binding energy and the electrostatic tunability of excitons in 2D group-VIB TMDs strongly suggest a new paradigm for the study of exciton physics. Moreover, they imply a particularly strong Coulomb interaction in 2D group-VIB TMDs due to the reduced dielectric screening in the 2D geometry,^{39,42} which will lead to interesting many-body phenomena.

Remarkable progress has been made in devices based upon 2D group-VIB TMDs. Monolayer MoS₂ field effect transistors at room temperature have shown high current on/off ratios, low standby power dissipation and reasonably good mobility, which significantly promoted the interest in these 2D materials for device applications.¹³ Various approaches in fabrication of high quality 2D TMD transistors have led to the steady progress in improving the mobilities in these devices.^{47–51} Light-emitting p-n junctions have also been created electrostatically within TMD monolayers by independent gating adjacent regions of the layer.^{52–55} Ambipolar transport in these devices is clearly demonstrated, and electroluminescence in the forward biased p-n junction has been observed. Interestingly, the electroluminescence from some devices is found to be circularly polarized, possibly a manifestation of unbalanced light emissions from the two valleys controlled by electric gating.^{55,56}

Nanostructures in 2D group-VIB TMDs are also being actively explored, including nano-flakes,^{57,58} nano-ribbons,^{59–70} grains and grain boundaries,^{16,17,71} lateral heterostructures,⁷¹ and quantum dots.^{72,73} In particular, on smooth edges or domain boundaries of TMD monolayers and bilayers, mid-gap metallic states are found with large density of states.^{16,19,57,58} These metallic states are catalytically active for hydrodesulfurization and hydrogen evolution reaction, and nano flakes of 2D group-VIB TMDs are of high interest for these catalytic applications.^{19,74–84}

The above are only a few selected examples of the appealing features of 2D group-VIB TMDs, which are being discovered at a rapid pace. They have made these 2D materials an ideal platform to explore a variety of applications, as well as an excellent building block for van der Waals heterostructures that may lead to even richer physics.⁴

Underlying the extraordinary properties of 2D group-VIB TMDs are their electronic structures. While 2D group-VIB TMDs are widely considered as the gapped counterpart of graphene with the same hexagonal 2D lattice, the electronic structures are much more complicated. At least a total of eleven atomic orbitals in each unit cell – five d-orbitals from the metal atom and six p-orbitals from the two chalcogen atoms – are considered relevant in various contexts. The strong spin-orbit coupling (SOC) inherited from the d-orbitals introduces more complexity as well as interesting spin-dependence in the electronic and optical properties. Unlike graphene where a single-orbital tight-binding (TB) model well describes the electronic structure of the active bands over the entire BZ, theoretical models have been developed for 2D group-VIB TMDs at different levels with their advantages and limitations, owing to their complex electronic structures. Momentum space $k\cdot p$ models aim at describing the low energy electrons and holes near the band edges in the 2D bulk, and the real space TB models are indispensable for calculations of mesoscopic transport as well as the study of nanostructures such as quantum dots and nano-ribbons. Models involving more atomic orbitals may give better description of the bands over larger k -space regions, while simpler models that capture the essential physics are advantageous in the theoretical studies of complex phenomena. In light of the rapidly growing research activities, a review that gives a comprehensive account of the electronic structures and the theoretical models in 2D group-VIB TMDs, sorting out the origin of the observed extraordinary properties, is necessary.

This review will focus mainly on the development in the theoretical understanding of electronic structures in the 2D bulk of group-VIB TMDs including the band dispersions, electronic and optical band gaps, the spin-orbit splitting and spin/pseudospin configurations of the energy bands, the orbital compositions and symmetries of the wave functions, the selection rules for the optical inter-band transition, interlayer hopping, heterojunctions, as well as the Berry phase related properties of Bloch electrons including the Berry curvature and orbital magnetic moment. We will also give an overview of the various $k\cdot p$ models

and TB models developed so far in describing these electronic structures. Our discussions will focus on the four most extensively studied TMDs: MoS₂, WS₂, MoSe₂, and WSe₂ (hereafter TMD refers to these compounds if not stated otherwise).

2 Electronic structure

The electronic structures of 2D TMDs are largely determined by their crystal structures. Bulk TMDs have been studied decades ago,^{85–95} which are known to crystallize in three different layered structures, *i.e.* 1T, 2H (*cf.* Fig. 1d) and 3R (*cf.* Fig. 1e). 1T is not as stable as the 2H and 3R phases for the four group-VIB TMDs we are focusing on.⁹⁶ For the 2H and 3R phases, the monolayer has the identical structure and the difference lies in the stacking order of the monolayers in the layered structures. The monolayer as the elementary building block in fact consists of three atomic planes. The top and bottom planes are chalcogen atoms in a triangular lattice structure, and the middle plane is another triangular lattice of metal atoms, in trigonal prismatic coordination (*cf.* Fig. 1b). The three atomic layers together form a 2D hexagonal lattice, with the A-sublattice being the metal atom per site and B-sublattice being the two chalcogen atoms per site. The 2H phase of the bulk crystal has the hexagonal symmetry, having two monolayers per repeat unit, where the neighboring monolayers are 180° rotation of each other, with the A site of one layer right on top of the B site of the other, and *vice versa* (*cf.* Fig. 1d). The 3R phase has the rhombohedral symmetry, having three layers per repeat unit, where the neighboring layers are translation of each other (*cf.* Fig. 1e). First-principles calculations show that bilayer in 2H stacking is more stable than the 3R stacking.⁹⁷ Thin film TMDs exfoliated from the natural crystals are mostly 2H stacking in the existing studies, even though 3R stacking is possible, albeit not frequently.^{97,98}

Apart from MS₂ and MSe₂, bulk MoTe₂ can also exist in the 2H phase (known as α -MoTe₂) below ≈ 815 °C, while at temperature higher than 900 °C it exists as metallic β -MoTe₂ with monoclinic structure.^{10,99} The α -MoTe₂ monolayer has been experimentally realized.³ Bulk WTe₂ exists stably as metallic Td-WTe₂ with octahedral coordination, but not in the 2H phase.^{7,8} The 2D form of 2H-WTe₂ might exist on some substrate, but has not been realized. Most properties of the 2D MS₂ and MSe₂ to be discussed apply to 2D 2H-MoTe₂ and 2H-WTe₂, except that the two ditellurides have a smaller band gap and a larger spin-orbit effect than the corresponding disulfides and diselenides.¹⁰⁰

When group-VIB TMDs are thinned down to a monolayer, a critical change is the crossover from the indirect band gap in bulk to the direct band gap in monolayer form. Density functional theory (DFT) calculations have first pointed to a direct band gap in monolayer WSe₂¹⁰¹ and MoS₂,^{5,102} located at the corners of the hexagonal BZ, *i.e.* the $\pm K$ points. The WS₂ monolayer was also studied a decade ago by both an angle-resolved photoemission spectroscopy (ARPES) experiment and DFT calculations, which identified its valence band maximum at the $\pm K$ points but did not draw a conclusion of direct band gap.^{103–105} The first experimental

evidence of the direct band gap is from the PL measurements, where monolayers exhibit orders of magnitude increase in the quantum efficiency of luminescence compared to the bulk and multilayers.^{11,12}

Another critical difference between bulk crystals and monolayer is the symmetry. The 2H bulk is inversion symmetric, as shown in Fig. 1d. However, when thinned down to a monolayer, the unit cell becomes half of its bulk counterpart, and inversion symmetry is broken. The crystal symmetry reduces from the space group D_{6h}^4 for the 2H bulk to the group D_{3h}^1 for a monolayer. The presence of inversion symmetry in the bulk and films with even number of layers and the absence of inversion symmetry in films with odd number of layers can be best illustrated by a spatial contrast image of second harmonic generation from a flake with thickness variations.¹⁰⁷

In the layered structures, the van der Waals coupling between neighboring monolayers is much weaker compared to the covalent bonds that form the monolayer. Below, we will focus first on the monolayers which are of most current interest because of their direct band gap. Then we will focus on the bilayers and discuss how the interlayer coupling can affect the electronic structures. These together will form the basis to understand the electronic structures of the multilayer thin films as well as complex van der Waals heterostructures.

2.1 Monolayers

Critical points and orbital compositions of energy bands. Critical points refer to the extrema or saddle points of the energy bands. They give rise to van Hove singularities in the electronic density of states, and play crucial roles in determining the transport and optical phenomena. We consider here the active bands only, *i.e.* the top valence band (VB) and the lowest conduction band (CB). In monolayers, the conduction band minimum (CBM) and the valence band maximum (VBM) are both located at the corners of the first BZ. The six corners belong to two inequivalent groups denoted by K and $-K$ points respectively, where each group has three equivalent corners related to each other by reciprocal lattice vectors (*cf.* Fig. 1c). The energetically degenerate but inequivalent band extrema at K and $-K$ constitute a discrete index of carriers, known as the valley index or pseudospin. Low-energy electrons and holes therefore have this extra valley degree of freedom in addition to spin. K and $-K$ transform into each other under the time reversal operation. Hereafter we use K_c and K_v to denote the CBM and VBM at the $\pm K$ points respectively. The calculated effective masses at K_c and K_v are in the order of $\sim 0.5m_0$ (m_0 is the free electron mass) while actual values differ between calculations depending on the lattice constants and approximation used.^{108–111}

The CB also has six local minima at the low symmetry Q points (*cf.* Fig. 1c and 2a, also referred to as A points in some literature^{112,113}), while the VB has a local maximum at the Γ point, which are referred to as Q_c and Γ_v respectively hereafter. These critical points are also important because they are energetically close to K_c and K_v respectively, and in cases such as under strain or in multilayers, Q_c may become the global CBM or Γ_v the global VBM. K and Γ are high symmetry points

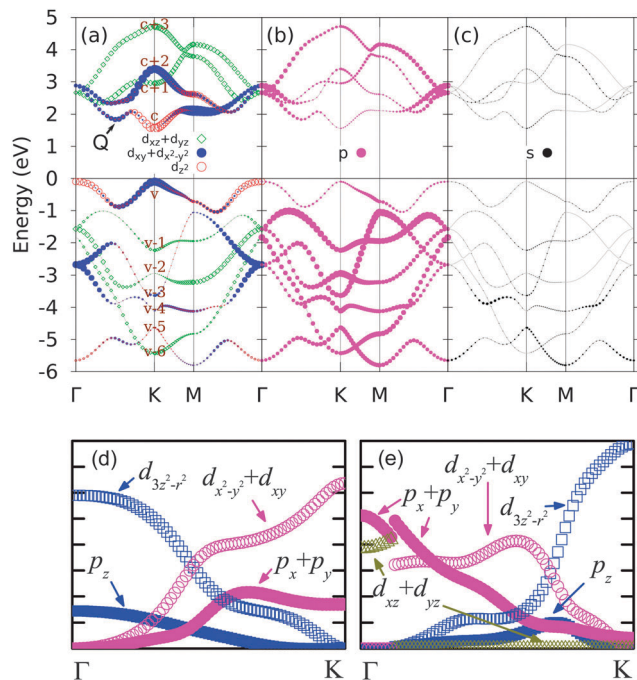


Fig. 2 (a)–(c) Orbital projected band structures for the MoS₂ monolayer from first-principles calculations without SOC. States at the K points are labelled as from $v - 6$ to $c + 3$. Fermi energy is set to zero. Symbol size is proportional to its population in corresponding state. (a) Contributions from Mo-d orbitals: blue dots for d_{xy} and $d_{x^2-y^2}$, red open circles for d_{z^2} , and green open diamonds for d_{xz} and d_{yz} . (b) Total p orbitals, dominated by S atoms. (c) Total s orbitals. (d)–(e) Orbitally resolved contributions of Se and W as a function of k along the line Γ – K for monolayer WSe₂: (d) top valence band; (e) lowest conduction band. (in arbitrary units). (a)–(c) Adapted with permission from ref. 100. Copyright 2013, American Physical Society. (d)–(e) Reproduced with permission from ref. 106. Copyright 2011, American Physical Society.

invariant under the C_3 operation (the rotation by $2\pi/3$ around the z axis). With this discrete rotational symmetry, the dispersions in the neighborhood of these critical points are anisotropic with the three-fold rotational symmetry (*i.e.* trigonal warping). Interestingly, the trigonal warping, while not large, may lead to a new possibility of generating valley and spin currents that are second order to the electric bias or temperature gradient.⁵⁶ The six Q_c valleys can be divided into two groups: Q and $-Q$. The C_3 operation transforms the three Q (or $-Q$) valleys into each other, while Q and $-Q$ are related by time reversal operation.

First-principles calculations find that, in monolayers, the 4 bands above the band gap and the 7 bands below the band gap are predominantly from the M-d orbitals and X-p orbitals. Other orbitals such as M-s, p and X-s have negligible contribution. There is perfect agreement between the first-principles bands and the Wannier bands constructed using only M-d and X-p orbitals.^{114,115} Orbital compositions of the bulk bands of TMDs are similar to those of monolayers.^{90,94} Fig. 2a–c shows the orbital compositions of the MoS₂ monolayer and Fig. 2d and e shows those of the WSe₂ monolayer.

For monolayers, the first-principles calculations also find that the band-edge states at K_c and K_v are predominantly from the M-d_{x²-y²}, d_{xy}, d_{z²} orbitals, with some mixture of X-p orbitals

Table 1 Orbital compositions of Bloch states at the conduction band critical points K_c and Q_c , and valence band critical points K_v and Γ_v in monolayer TMDs

State	Majority of orbitals	Minority of orbitals
K_c	M-d _{z²}	X-p _x , p _y
K_v	M-d _{x²-y²} , d _{xy}	X-p _x , p _y
Q_c	M-d _{x²-y²} , d _{xy}	M-d _{z²} , X-p _x , p _y , p _z
Γ_v	M-d _{z²}	X-p _z

(*cf.* Table 1).^{5,100,101,106,116–118} For wavefunctions at Q_c and Γ_v , the contributions from the X-p_z orbitals become significant. In fact, the X-p_z composition at Q_c and Γ_v play an important role in the crossover from the direct to indirect band gap from monolayer to bulk, because the close distance between X-p_z orbitals from neighbouring layers leads to large hopping, which changes the energy of Q_c and Γ_v substantially.^{102,118}

Even though first-principles calculations have provided valuable insight into the electronic structures of TMD monolayers, we emphasize that caution should be applied when interpreting the obtained results, *e.g.* the band-edge locations, especially when no experimental data are available. First-principles calculations have found that the energy separations between Q_c and K_c and between Γ_v and K_v depend sensitively on the lattice constant. It's well known that GGA (LDA) exchange–correlation functional overestimates (underestimates) the lattice constant in the energy minimization process of first-principles calculations. Hence the lattice constant determined by GGA (LDA) will introduce artificial tensile (compressive) strain, which may sometimes give conflicting results. For example, GGA calculations without SOC for a MoS₂ monolayer give an indirect gap with Γ_v higher than K_v by 4 meV, with the GGA lattice constant of 3.19 Å compared to the bulk experimental value 3.16 Å.^{100,109} Similarly, LDA gives indirect band gap for MoSe₂ and WSe₂ with Q_c lower than K_c .^{100,117,119} In addition to the lattice constant, there are other details that affect the calculated monolayer band structure, such as the GW (quasi-particle self-energy correction) method,^{120–122} hybrid functional, pseudopotential, and SOC. Turning on SOC, even in a GGA case, will correct the MoS₂ monolayer from an indirect to direct gap. Some GW calculations show that the MoS₂ monolayer has an indirect gap with CBM at Q_c ,^{109,123} while others give a direct gap.^{39,124} The inclusion of the 4s (for Mo) and 5s (for W) semi-core electrons is found to be crucial to obtain the direct gap.¹²⁴

Symmetry of band-edge wavefunctions. At the $\pm K$ points, the wave-vector group is C_{3h} whose generators are C_3 and σ_h (the mirror reflection about the xy plane across the M atoms). C_{3h} is an Abelian group and has only one-dimensional irreducible representations. This makes all the Bloch states at K nondegenerate, which have to be eigenstate of both C_3 and σ_h . The σ_h symmetry divides the five M-d orbitals into two sets: the even set $\{d_{z^2}, d_{x^2-y^2}, d_{xy}\}$ and the odd set $\{d_{xz}, d_{yz}\}$. X-p orbitals above and below the M-atom plane can also be arranged in terms of linear superpositions with odd and even σ_h symmetry respectively. When SOC is not considered, orbitals in the even set can not couple with those in the odd set. To be eigenstate of C_3 , orbitals have to combine chirally in spherical harmonic form,

Table 2 Symmetry and orbital compositions of Bloch states ψ_n at the K point in monolayer TMDs. The label n of the states follows from Fig. 2a. Only the dominant (in bold) and the secondary orbital compositions are shown. γ_{σ_h} is the eigenvalue (or mirror parity) of σ_h , $\gamma_{C_3}^{\rho}$ is the eigenvalue of C_3 (i.e. $C_3\psi_n = \gamma_{C_3}^{\rho}\psi_n$) and ρ is the rotation center located at M, X, or h (cf.

Fig. 1a). $\omega \equiv e^{i\frac{2\pi}{3}}$. The orbital compositions and $\gamma_{C_3}^{\rho}$ all correspond to the states at K in the lattice orientation shown in Fig. 1a, and the $-K$ states are their complex conjugates

n (in ψ_n)	Mo-d	S-p	γ_{σ_h}	$\gamma_{C_3}^M$	$\gamma_{C_3}^X$	$\gamma_{C_3}^h$
c + 3	d₊₁	p ₀	-1	ω^*	1	ω
c + 2	d₋₂	p ₀	+1	ω^*	1	ω
c + 1	d₋₁	p ₊₁	-1	ω	ω^*	1
c	d₀	p ₋₁	+1	1	ω	ω^*
v	d₊₂	p ₊₁	+1	ω	ω^*	1
v - 1	d₊₁	p ₀	-1	ω^*	1	ω
v - 2	—	p₋₁	-1	1	ω	ω^*
v - 3	d₋₂	p ₀	+1	ω^*	1	ω
v - 4	d₊₂	p₊₁	+1	ω	ω^*	1
v - 5	d₀	p₋₁	+1	1	ω	ω^*
v - 6	d₋₁	p₊₁	-1	ω	ω^*	1

i.e. $d_{\pm 2} = \frac{1}{\sqrt{2}}(d_{x^2-y^2} \pm id_{xy})$, $d_{\pm 1} = \frac{1}{\sqrt{2}}(d_{xz} \pm id_{yz})$, $d_0 = d_{z^2}$, $p_{\pm 1} = p_x \pm ip_y$, and $p_0 = p_z$. Under rotation about the atomic center of each orbital, these orbitals transform as

$$C_3\alpha_m = e^{-\frac{2m\pi}{3}}\alpha_m, \quad (\alpha = p, d; m = 0, \pm 1, \pm 2). \quad (1)$$

It should be noted that the action of C_3 on the Bloch states includes rotations of both the constructing atomic orbitals and the plane wave component in the Bloch functions.^{22,25,73} In Table 2, we list the main orbital compositions and the eigenvalues of both σ_h and C_3 for all the Bloch states at the K point. The corresponding eigenvalues and orbital compositions at the $-K$ point are simply the complex conjugate since K and $-K$ are time reversals of each other. We emphasize that the eigenvalue, $\gamma_{C_3}^{\rho}$, of C_3 rotation depends on the position of the rotation center, ρ , which can be M, X, or the h position (the hollow center of the hexagon formed by M and X, cf. Fig. 1a).⁷³ $\rho = M$ is used in the symmetry analysis of ref. 100, while $\rho = h$ is used in ref. 25 and 125. The dependence of C_3 eigenvalues of the Bloch states on the choice of rotation center can have important consequences, for example, it gives rise to sensitive dependence of intervalley coupling strength on the central position of a lateral confinement potential that also has the C_3 symmetry.⁷³

Valley optical selection rule. One of the most interesting properties of the TMD monolayers is the valley dependent circularly polarized selection rules for the optical direct band gap transitions at the $\pm K$ points.^{22,23} This simply follows from the C_3 eigenvalues of the Bloch states at the $\pm K$ points. We can establish the following identity for the interband optical transition matrix element:

$$\begin{aligned} \langle \psi_f | \hat{P}_{\pm} | \psi_i \rangle &\equiv \langle \psi_f | C_3^{-1} C_3 \hat{P}_{\pm} C_3^{-1} C_3 | \psi_i \rangle \\ &= \langle C_3 \psi_f | C_3 \hat{P}_{\pm} C_3^{-1} | C_3 \psi_i \rangle \\ &= e^{i\frac{2\pi}{3}(m_f - m_i \mp 1)} \langle \psi_f | \hat{P}_{\pm} | \psi_i \rangle. \end{aligned} \quad (2)$$

ψ_f and ψ_i are the Bloch states at K with $C_3 \psi_f = e^{-i\frac{2m_f\pi}{3}} \psi_f$, $C_3 \psi_i = e^{-i\frac{2m_i\pi}{3}} \psi_i$, where m_f and m_i are integers (cf. Table 2). \hat{P}_{\pm} is the momentum operator, $\hat{P}_{\pm} = \hat{P}_x \pm i\hat{P}_y$ and $C_3 \hat{P}_{\pm} C_3^{-1} = e^{\mp i\frac{2\pi}{3}} \hat{P}_{\pm}$. The quantity $|\langle \Psi_f | \hat{P}_{\pm} | \Psi_i \rangle|^2$ characterizes the oscillator strength of the interband transition with light of σ_{\pm} circular polarization. A nonzero $\langle \Psi_f | \hat{P}_{\pm} | \Psi_i \rangle$ requires $e^{i\frac{2\pi}{3}(m_f - m_i \mp 1)} = 1$, i.e. $(m_f - m_i \mp 1$ modulo 3) = 0. This is the azimuthal selection rule for allowed interband optical transitions. We note that the values of m_f and m_i in eqn (2) depend on the choice of rotation center, but the value $(m_f - m_i$ modulo 3) does not (cf. Table 2). The selection rule between the lowest conduction and top valence bands is of particular interest. According to Table 2, the direct band gap optical transition is allowed at K ($-K$) by the $\sigma_+(\sigma_-)$ polarized light only (cf. Fig. 3e). Under time reversal operation, K is transformed to $-K$, and σ_- is transformed to σ_+ , so this selection rule does respect the time reversal symmetry. Inversion operation also transforms K to $-K$, but it leaves the light circular polarization unchanged. Thus the valley dependent selection rule conflicts with inversion symmetry, the breaking of this symmetry is the necessary condition for having such a selection rule.^{22,23} While the above analysis is applicable to the high symmetry $\pm K$ points only, first-principles calculations have shown that the selection rule in fact holds approximately true in a large neighbourhood of $\pm K$ points.²⁵

The valley optical selection rule makes possible optical pumping and detection of valley polarization. Circularly polarized light can selectively inject photocarriers into one of the valleys, while valley polarization of electron-hole pairs will manifest as circularly polarized luminescence upon the electron-hole recombination. Initial experimental evidence of the valley optical selection rule come from the polarization resolved PL measurement where the light emission is found to have the same circular polarization as that of the excitation laser.²⁴⁻²⁶ Another unique consequence of the valley optical selection rule is the possibility to optically generate valley coherence.²⁷ Since linearly polarized photon is the coherent superposition of σ_+ and σ_- polarized photon, excitation by linearly polarized laser can optically inject an electron-hole pair in linear superposition at K and $-K$.

Electronic and optical band gaps and the excitonic effect.

The band gap generally refers to the energy difference between the CBM and VBM, which can be determined either by transport or optical measurements. However, the size of the band gap determined from the two types of measurement differs because of the excitonic effect that is present in the optical process. The band gap determined from the transport measurement is also known as electronic band gap. It characterizes single-particle excitations and is defined as the sum of the energies needed to separately tunnel an electron and a hole into the system.⁴⁶ In optical measurement, the absorption of a photon simultaneously creates an electron in the CB and a hole in the VB, which will bind through Coulomb interaction into an exciton. The energy required to create an exciton is then referred to as the optical band gap. Clearly, the difference between the electronic and optical band gaps corresponds to the binding energy of the exciton, which reflects the strength of the Coulomb interaction.

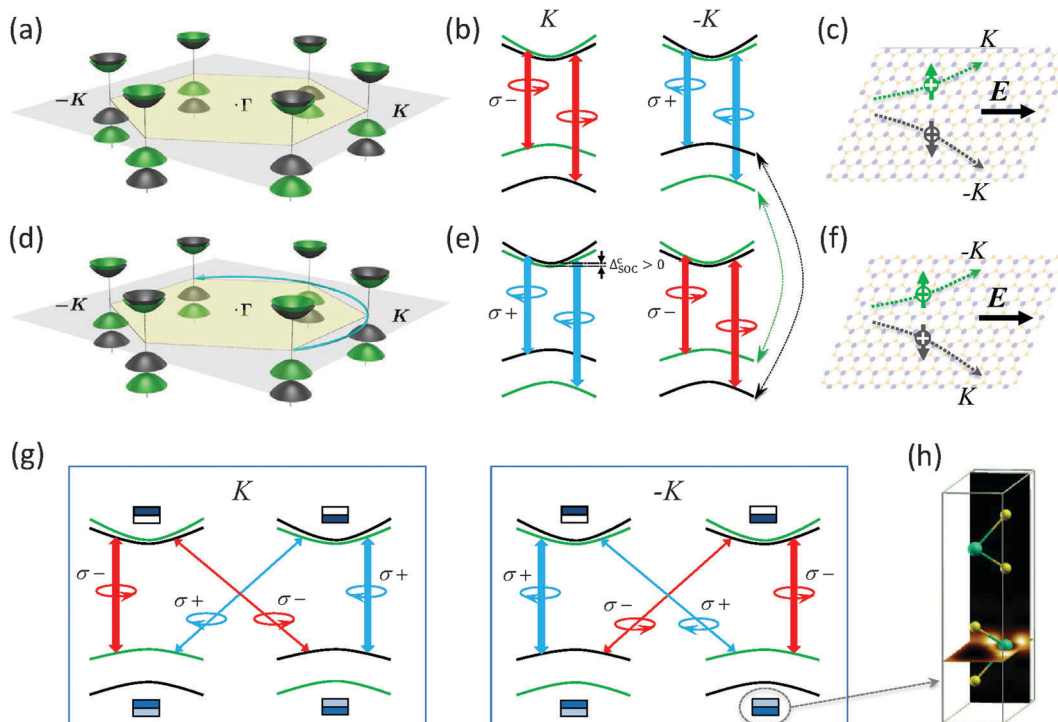


Fig. 3 Valley and spin physics in TMD monolayers and 2H stacked bilayers. (a) Schematics of the spin-valley coupled band edges in monolayer WX_2 . Black (green) color denotes spin-up (-down) bands. (b) Valley and spin dependent optical transition selection rules in monolayers. (c) Valley Hall effect due to the valley contrasting Berry curvature (cf. Fig. 4a and b). For holes, the valley Hall effect is also a spin Hall effect, as the spin and valley indices are locked at the VBM. (d)–(f) The same physics is shown for a WX_2 monolayer which is a 180° rotation of the one in (a)–(c). The rotation switches the K and $-K$ valleys, but leaves spin, Berry curvature, and light circular polarization unchanged. (a)–(f) Together illustrates the net effects in two decoupled monolayers of 2H stacking: (a) and (d) spin splitting with a valley- and layer-dependent sign; (b) and (e) valley circular dichroism cancels out in the two layers, while the spin circular dichroism remains; (c) and (f) valley Hall effect cancels out while the spin Hall effect remains. (g) Optical transition selection rules in the K and $-K$ valleys of 2H stacked coupled bilayers. The interlayer hopping (cf. dashed arrows between (b) and (e)) is largely quenched by the layer dependent spin splitting, so the Bloch states are predominantly residing in an individual layer (illustrated with the rectangular blocks where darker color denotes more occupation). Thick arrows denote the intralayer optical transitions, and thin arrows denote the interlayer transitions due to the residue small layer hybridization of the valence band states. (h) First-principles calculated electron density map for one valence band Bloch state in a coupled WS_2 2H bilayer. (b), (e) and (g) Adapted with permission from ref. 34. (h) Adapted with permission from ref. 107. Copyright 2013, Nature Publishing Group.

Optical band gaps of monolayer TMDs have been determined from PL measurements, as listed in Table 3. For all four group-VIB TMDs the band gaps fall into the visible frequency range, making them ideal systems to explore semiconductor optics and optoelectronic applications. The substrate and dielectric environment can change the value of the optical band gap by a few percent.^{11,12,126–131} In high quality MoSe_2 and WSe_2 samples, the neutral and charged excitons are found with a narrow PL linewidth of a few meV, while the separation between the neutral and charged excitons is 20–30 meV.^{27,37} This makes possible a reliable characterization of the temperature dependence of the optical gap, which can be well fitted by the standard semiconductor band gap dependence.³⁷

Table 3 Optical band gaps in TMD monolayers determined from PL experiments

	Gap
MoS_2	$1.83^{11}, 1.90^{12}$
WS_2	1.95^{107}
MoSe_2	1.66^{37}
WSe_2	1.64^{107}

Electronic band gap has also been measured using scanning tunneling spectroscopy (STS) and ARPES. For monolayer MoS_2 on highly ordered pyrolytic graphite (HOPG), STS measurements give an electronic band gap of 2.15 eV or 2.35 eV at 77 K depending on the choice of threshold value of tunneling current,^{45,132} while PL measurement on the same sample gives an optical gap of 1.93 eV at 79 K. For WSe_2 and WS_2 monolayers on HOPG, the STS measurement shows an electronic band gap of 2.51 eV and 2.59 eV respectively at 77 K.¹³² For monolayer MoSe_2 grown by molecular beam epitaxy (MBE) on bilayer graphene, the STS-determined electronic band gap is 2.18 eV at 5 K, while PL shows the optical gap of 1.63 eV at 77 K.⁴⁶ MoSe_2 grown by MBE on a HOPG substrate shows a similar electronic band gap of 2.1 eV in the STS measurement.¹⁹ In the interpretation of the STS measured gap, a possible complication is that Γ_v and Q_c have much larger weight in the scanning tunneling spectra than K_v and K_c ,⁴⁶ due to the larger density of states as well as a larger tunneling coefficient at Γ_v and Q_c . The latter is due to the fact that the wavefunctions at Γ_v and Q_c have a nonnegligible component from $\text{X}-\text{p}_z$ orbitals, which are closer to the STM tip. This may obscure the attribution of the band edge.

ARPES measurement on a heavily doped MBE grown MoSe₂ monolayer has reported a much smaller band gap of ~ 1.58 eV,¹⁸ implying a large band gap renormalization due to the screening effect by the carriers.⁴⁶

The difference between the measured electronic and optical band gaps point to a large exciton binding energy of hundreds of meV in monolayer TMDs. An exciton binding energy in the range of 0.3–0.7 eV has also been inferred in the WX₂ monolayer from spectral features in two-photon absorption and reflectance measurement which are attributed as excitonic excited states.^{40–43} Moreover, the charging energy, *i.e.* energy difference between the neutral exciton and charged exciton in the PL, is measured to be in the range of 20–40 meV,^{27,36,37} which is consistent with the above binding energy for 2D excitons. These all point to exceptionally strong Coulomb interaction, due to the large effective masses of both electrons and holes and the reduced screening in the 2D limit.^{39,46}

There have been remarkable efforts in first-principles calculations of band gaps and the excitonic effects on TMD monolayers.^{38,39,108,109,123,133–135} DFT calculations underestimate the electronic band gap significantly. The GW method beyond DFT and based on many-body perturbation theory is generally used to obtain the electronic band gap. To calculate the exciton binding energy, Bethe-Salpeter equation (BSE)^{136,137} is solved based on the GW method to obtain the optical absorption spectra and then the exciton binding energy is obtained by subtracting the optical transition energy from the electronic band gap. The exciton binding energy from these calculations agrees in the order of magnitude with the experiments. For monolayer MoSe₂, the experiments and first-principles calculations agree quantitatively well on the electronic band gap and the exciton binding energy.⁴⁶ However, the obtained exciton binding energy depends on the computational details. *k* sampling not dense enough overestimates the exciton binding energy,^{109,123,138} while finite interlayer separation underestimates the exciton binding energy.^{123,134} The underestimation from finite interlayer separation can be solved by using extrapolation as the interlayer separation going infinite¹³⁴ or by using truncated Coulomb interaction,^{39,123} and the latter method is considered more reliable.¹²³ In addition, including the electron–phonon interaction will result in red shift of the absorption peak obtained in BSE and affect the exciton binding energy consequently.¹³⁹ A rather interesting observation from these first-principles calculations is that the GW correction and the exciton binding energy have a comparable value, giving rise to the accidental agreement between the DFT calculated gap and the measured optical gap.^{39,109}

The exciton Bohr radius calculated by the GW-BSE method is on the order of 1 nm,^{38,39,135} still a few times larger than the lattice constant. So the exciton in monolayer TMDs is of a mixed character: the binding energy is comparable to typical Frenkel excitons, while the wavefunction of the electron–hole relative motion is largely of the Wannier type, extending over a large number of unit cells. Correspondingly, the exciton wavefunction is well localized in momentum space. A bright exciton that can emit photon has its electron and hole constituents both localized in the *K* or $-K$ valleys. These valley excitons well

inherit the valley optical selection rule of the band-to-band transition. Namely, the *K* ($-K$) valley exciton can be interconverted with the $\sigma_+(\sigma_-)$ photon. This selection rule forms the basis of the recently demonstrated optical generation of excitonic valley pseudospin polarization and coherence.^{24–27} The strong Coulomb interaction in monolayer TMDs also gives rise to pronounced exchange interaction between the electron and hole constituents of the exciton, which strongly couples the valley pseudospin of exciton to its center of mass motion.¹⁴⁰

Spin-orbital interaction and spin-valley locking. TMDs have a strong SOC originated from the d orbitals of the metal atoms. The form of SOC induced spin splitting of bands in monolayers can be fully determined by symmetry analysis. The first constraint is from σ_h , the mirror reflection symmetry about the metal atom plane, which dictates a Bloch state and its mirror reflection to have identical energy. The σ_h mirror reflection of an in-plane spin vector is its opposite, while the mirror reflection of an out-of-plane spin vector is itself. Thus spin splitting is allowed in the out-of-plane (*z*) direction only, where the spin expectation value of the Bloch states is either along the $+z$ or $-z$ direction. Secondly, the time reversal symmetry dictates the spin splittings at an arbitrary pair of momentum space points *k* and $-k$ to have identical magnitude but opposite sign.³⁴ In the neighborhood of *K* and $-K$, the SOC then manifests as an effective coupling between the spin and valley pseudospin, *i.e.* with the sign of the spin splitting conditioned on the valley pseudospin. We note that inversion symmetry would impose a conflicting constraint from that of the time reversal symmetry, so inversion symmetry breaking in the monolayer is the necessary condition for having this spin–valley coupling.

First-principles calculations with GGA find that the VB at the *K* point has a SOC of ~ 0.15 eV for the MoX₂ monolayer and ~ 0.45 eV for the WX₂ monolayer, while the HSE hybrid functional and GW calculations give slightly larger values (*cf.* Table 4).^{23,106,108} Experimental evidence for such a giant SOC is reflected in PL measurements where two peaks, attributed as excitons with the holes from the two split-off spin subbands respectively, are seen with an energy separation in agreement with the VB spin splitting at $\pm K$.^{12,107} Lately, the ARPES measurement of MBE grown MoSe₂ gives a direct evidence of the VBM SOC splitting of ~ 0.18 eV,¹⁸ in agreement with the calculations. Because of this giant SOC, the VBM in monolayer TMDs has the spin index locked with the valley index, *i.e.* valley *K* ($-K$) has only the spin up (down) holes (*cf.* Fig. 3a). Another important consequence of the SOC is that the valley dependent optical selection rule becomes a spin

Table 4 SOC splitting at K_v and K_c in TMD monolayers from first-principles calculations

	Δ_{SOC}^v (eV)			Δ_{SOC}^c (eV)	
	GGA	HSE ¹⁰⁸	GW ¹⁰⁸	GG ¹⁰⁰	
MoS ₂	0.148, ^{100,106} 0.146 ¹⁰⁸		0.193	0.164	-0.003
WS ₂	0.430, ¹⁰⁰ 0.426, ¹⁰⁶ 0.425 ¹⁰⁸		0.521	0.456	0.029
MoSe ₂	0.184, ¹⁰⁰ 0.183 ^{106,108}		0.261	0.212	-0.021
WSe ₂	0.466, ¹⁰⁰ 0.456, ¹⁰⁶ 0.461 ¹⁰⁸		0.586	0.501	0.036

dependent one as well.²³ For example, σ_+ polarized light still excites only the K valley, but depending on the light frequency, it can either resonantly excite spin up or down carriers (*cf.* Fig. 3e).

The CB at $\pm K$ also has the spin splitting with the same symmetry-dictated form as the VB. The magnitude, however, is much smaller, about a few meV for MoS₂ and tens of meV for other TMDs from first-principles calculations (*cf.* Table 4),^{72,100,115,116,125,133,141–144} and some experimental evidences of this SOC splitting has been reported recently.¹⁴⁵ The small CB SOC is due to the fact that the CB Bloch states at $\pm K$ are predominantly formed by the M-d₀ orbitals where the intra-atomic $L\cdot S$ coupling as the dominant contribution to SOC vanishes to the leading order. Interestingly, the first-principles calculation finds an overall sign difference of the CB splitting between MoX₂ and WX₂.¹⁰⁰ The CB splitting originates from the first order effect from the small X-p _{± 1} compositions, as well as the second-order coupling mediated by the remote conduction bands consisting of M-d _{± 1} orbitals (*cf.* Table 2).^{100,125,144} The two contributions to SOC have opposite sign and their competition leads to the sign difference between MoX₂ and WX₂.^{100,115}

For the Q_c valleys of the CB, sizable spin splittings are also found in the first-principles calculations.⁵⁶ The three Q ($-Q$) valleys have the same spin splitting as they are related by the C_3 rotation, while the splittings at Q and $-Q$ have opposite sign. In the neighborhood of Γ_v , the spin splitting has a quadratic dependence on the wavevector with a three-fold pattern for the sign.⁵⁶

Berry phase related properties. The Berry phase effect for a particle lies in the dependence of the internal structure on the dynamical parameter. In the context of Bloch electrons, it is the dependence of the periodic part of the Bloch function $u_{n,k}(\mathbf{r})$ on the wavevector \mathbf{k} .¹⁴⁶ The Berry curvature and orbital magnetic moment are two physical quantities that characterize the effect of Berry phase of electrons in the Bloch bands. The Berry curvature is defined as: $\Omega_n(\mathbf{k}) = i \left\langle \frac{\partial}{\partial \mathbf{k}} u_{n,k} \right| \times \left| \frac{\partial}{\partial \mathbf{k}} u_{n,k} \right\rangle$. In an applied electric field, the Berry curvature gives rise to an anomalous velocity $v_\perp = -\frac{e}{\hbar} \mathbf{E} \times \Omega(\mathbf{k})$, *i.e.* a Hall effect (*cf.* Fig. 3c and f). Thus, Berry curvature plays the role of a magnetic field in the momentum space. For the 2D crystal, Berry curvature is a pseudo-vector in the out-of-plane (z) direction, and its projection along the z axis is:

$$\Omega_n(\mathbf{k}) = - \sum_{n'(\neq n)} \frac{2\text{Im}\langle u_{nk}|v_x|u_{n'k}\rangle\langle u_{n'k}|v_y|u_{nk}\rangle}{(E_{n'}(\mathbf{k}) - E_n(\mathbf{k}))^2},$$

where v_{xy} is the velocity operator and $E_n(\mathbf{k})$ is the energy dispersion. In monolayer TMDs, a sizable Berry curvature is found in the neighborhood of the $\pm K$ points from theoretical modeling and first-principles calculations.^{21,23,25,114} As the K and $-K$ valleys are time reversal of each other, the Berry curvature must have opposite values at K and $-K$ (*cf.* Fig. 4a and b). The Berry curvature is invariant under spatial inversion that also transform K and $-K$ into each other. Thus, inversion symmetry breaking is the necessary condition for having the valley contrasting Berry curvature.

By the valley contrasting Berry curvature, an in-plane electric field can drive the carriers at the K and $-K$ valleys to the opposite transverse edges (*cf.* Fig. 3c and f). Such a valley dependent Hall effect is an analog of the spin Hall effect, but with the valley pseudospin playing the role of spin. The valley Hall effect in a monolayer MoS₂ transistor has been reported recently in experiments.²⁹ For hole doped systems, because the spin is locked with the valley index at the VBM, the valley Hall effect is also accompanied by a spin Hall effect with the same Hall conductivity (up to a proportionality constant). For the electron doped case, the spin up and down electrons in the same valley have slightly different Berry curvatures (*cf.* Table 6), which also gives rise to a finite, albeit smaller, spin Hall effect.^{23,114} This is illustrated in Fig. 4c and d, which shows the first-principles calculated spin Berry curvature

$$\Omega_n^s(\mathbf{k}) = - \sum_{n'(\neq n)} \frac{2\text{Im}\langle \psi_{nk}|j_x|\psi_{n'k}\rangle\langle \psi_{n'k}|v_y|\psi_{nk}\rangle}{(E_{n'} - E_n)^2},$$

j_x being the spin current operator defined as $\frac{1}{2}(\hat{s}_z v_x + v_x \hat{s}_z)$. At the CBM and VBM where spin up and down states are not mixed, the spin Berry curvature is simply given by $\Omega^s(\mathbf{k}) = s_z \Omega(\mathbf{k})$. Fig. 4c and d also shows finite spin Berry curvature near Γ_v where the spin Hall effect is also expected.

Berry curvature is in general accompanied by the orbital magnetic moment, which can be viewed as the self-rotating motion of the electron wavepacket.¹⁴⁶ Similar to the spin magnetic moment, the orbital magnetic moment will lead to Zeeman shift in a magnetic field. The time reversal symmetry also requires the orbital magnetic moment to have identical magnitude but opposite signs at K and $-K$. Therefore, similar to the spin, the two valley pseudospin states are associated with opposite magnetic moment, making possible magneto-control

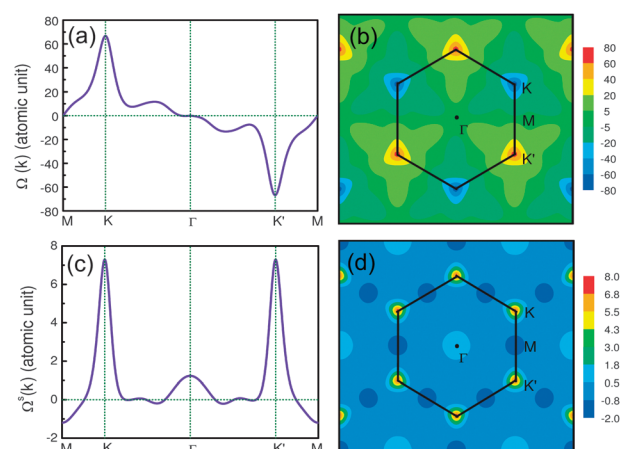


Fig. 4 (a)–(b) First-principles calculated Berry curvature in the MoS₂ monolayer. (a) Shows the curvature along the high-symmetry lines, and (b) shows the distribution in the 2D k -plane, in the atomic unit (Bohr²). (c)–(d) First-principles calculated spin Berry curvature in the MoS₂ monolayer. The plots are for the sum of $\Omega_n(\mathbf{k})$ (or $\Omega_n^s(\mathbf{k})$) from all valence bands, but the dominant contribution is from the top valence band of interest. Reproduced with permission from ref. 114. Copyright 2012, American Physical Society.

of the pseudospin dynamics.^{30–32} The valley contrasting Berry curvature and magnetic moment, as well as the valley and spin dependent optical selection rules, make TMD monolayers an ideal platform for investigating spintronics and valleytronics.

Strain effects on band structures. Strain can tune various physical properties in monolayer TMDs including the band gap, band edge locations, effective mass, phonon mode, and magnetism, as shown in theoretical^{38,66,109,117,119,147–157} and experimental studies.^{129,152,158–160} First-principles calculations show that biaxial tensile strain in the MoS₂ monolayer lifts the energies of Γ_v and Q_c points, and under moderate strain (<2%) the band gap can cross from the direct one ($K_v \leftrightarrow K_c$) to an indirect one ($\Gamma_v \leftrightarrow K_c$).^{109,147,148,151} The calculations also find that the band gap decreases with the biaxial tensile strain and the monolayer may become a metal under a larger strain of 8–10%.^{148,149,151} In contrast, calculations find that biaxial compressive strain in a MoS₂ monolayer lowers the energies of Γ_v and Q_c points, and the band gap also crosses to an indirect one ($K_v \leftrightarrow Q_c$, different from the tensile case). Meanwhile, the band gap increases with compressive strain up to a ~2% strain strength^{66,117,147} and then decreases with larger strain until it becomes metallic.¹⁵¹ Other TMD monolayers have qualitatively the same behaviors under biaxial strain.^{117,119,147,149} Uniaxial strain on TMD monolayers are also studied using first-principles calculations, where similar but quantitatively smaller effects are found.^{117,149} Experiments show that uniaxial tensile strain results in red shift of both PL and Raman peaks,^{129,158,159} consistent with first-principles calculations.

Interesting strain effects on valley pseudospin properties in monolayer TMDs have also been predicted. Uniaxial tensile strain breaks the C_3 symmetry and results in an in-plane Zeeman field on the valley pseudospin of excitons.¹⁴⁰ A moderate strain (~1%) can lead to a sizable valley pseudospin splitting of a few meV at zero exciton center-of-mass momentum. It has also been predicted that inhomogeneous shear strain may lead to a valley-contrasting effective magnetic field in the out-of-plane direction for carriers, and spin polarized Landau levels can develop.^{161–164} These all point to interesting possibilities towards mechanical control of spin and valley pseudospin of excitons and carriers.

2.2 Bilayers and heterostructures

First-principles calculations find that 2H stacking is the most stable configuration for homostructure bilayer TMDs.^{165–167} In the 2H stacking, the upper layer is the 180° rotation of the lower one, which is an operation that switches the two valleys (cf. Fig. 3a–f). Thus the valley dependent physical properties of each monolayer, including the valley optical circular dichroism and valley Hall effect, would average to zero in the pristine 2H bilayer (cf. Fig. 3), as required by the restoration of inversion symmetry (cf. Fig. 1d). Nevertheless, a perpendicular electric field can break the inversion symmetry, and leads to the emergence of valley circular dichroism and a valley Hall effect.^{22,28,33} This makes possible a controllable way to tune the valley physical properties by changing the symmetry of the system. Preliminary evidence for such tunability has been reported in the MoS₂ bilayer where the PL circular polarization

as a signature of the valley circular dichroism can be switched on and off by the interlayer bias.³³ The PL circular polarization has also been used to indicate the inversion symmetry breaking in the MoS₂ bilayer.^{97,98} Non-zero PL circular polarization is generally observed in as-prepared 2H MoS₂ bilayer in the absence of external gating, implying the existence of a perpendicular electric field from the substrate effect, consistent with the presence of large n-doping.^{26,33}

Band edges. The first-principles calculated band structures of TMD bilayers, in particular the band edges and band gaps, depend on the parameters and approximations used (cf. Table 5). Lattice constant and interlayer distance are the two geometry parameters affecting the band edges most. DFT without the van der Waals correction will overestimate the interlayer distance in the GGA calculations^{165,170} (may also underestimate a little in LDA^{166,171}), resulting in too small interlayer interactions to describe the bilayers reasonably. First-principles calculations of bilayer MoS₂ with geometry parameters using measured bulk values and the van der Waals relaxation results (PBE-D2¹⁷⁴) lead to different indirect band gaps of $\Gamma_v \leftrightarrow Q_c$ and $\Gamma_v \leftrightarrow K_c$ respectively.¹⁷⁰ For WS₂ and MoSe₂ bilayers, larger interlayer distance, *i.e.* the van der Waals relaxed one compared to the bulk one, will change the VBM from Γ_v to K_v .³⁴ Other computational

Table 5 Conduction and valence band edges of TMD bilayers from first-principles calculations

Bilayer	Band edge	Ref.
MoS ₂	$\Gamma_v \leftrightarrow Q_c$	11, 34, 113, 142, 167–171
	$\Gamma_v \leftrightarrow K_c$	66, 112, 133, 147, 151, 166, 165, 170, 172, 173
WS ₂	$\Gamma_v \leftrightarrow Q_c$	34, 107, 112, 113, 142, 147, 167, 170, 171
	$\Gamma_v \leftrightarrow K_c$	168
	$K_v \leftrightarrow Q_c$	34
MoSe ₂	$\Gamma_v \leftrightarrow Q_c$	34, 113, 138, 167, 170, 171
	$K_v \leftrightarrow K_c$	147
	$K_v \leftrightarrow Q_c$	34
WSe ₂	$K_v \leftrightarrow Q_c$	34, 101, 107, 113, 147, 167
	$\Gamma_v \leftrightarrow Q_c$	171
	$\Gamma_v \leftrightarrow K_c$	112

Table 6 Comparison of the Berry curvatures at VBM and CBM between the first-principles calculations (the first line) and the $k\cdot p$ model in ref. 23 (the second line) for monolayer TMDs. $\Omega_{v(c)\uparrow(\downarrow)}$ is the Berry curvature of the valence (conduction) band with spin $\uparrow(\downarrow)$, given in the unit of Bohr². Reproduced with permission from ref. 114. Copyright 2013, American Physical Society

	MoS ₂	MoSe ₂	WS ₂	WSe ₂
$\Omega_{v\uparrow}$	38.8	39.7	59.8	64.3
	35.3	36.5	55.4	60.0
$\Omega_{v\downarrow}$	31.6	30.0	34.9	34.7
	29.5	28.4	34.2	33.3
$\Omega_{c\uparrow}$	−35.7	−36.8	−54.7	−59.2
	−35.3	−36.5	−55.4	−60.0
$\Omega_{c\downarrow}$	−28.8	−27.3	−31.0	−30.8
	−29.5	−28.4	−34.2	−33.3

details such as the SOC, exchange correlation functional, pseudopotential, and GW may also give different results, *e.g.* including SOC can change the VBM of the WS₂ bilayer from Γ_v to K_v .^{107,113} The only direct evidence available are the ARPES studies which show the VBM at Γ_v for MoS₂ and MoSe₂ bilayers.^{18,175} More experimental studies are needed for determining the band edges and band gaps in bilayer TMDs under various conditions.

The sensitive band-edge dependence on the lattice constant and interlayer distance points to significant strain effects. The MoS₂ bilayer under in-plane biaxial strain is found to behave similarly to its monolayer counterpart: (i) band gap decreases with the increase of tensile strain; (ii) under compressive strain the gap first increases and then decreases; (iii) under large enough strain of either tension or compression, the bilayer can become metallic.^{66,151} Under out-of-plane compressive strain, TMD bilayers can also undergo semiconductor-to-metal transition.¹⁶⁵ In addition to strain, the perpendicular electric field can also decrease the band gap of TMD bilayers near linearly.^{166,170,176}

Interlayer hopping. The crossover from a direct band gap at the monolayer to an indirect band gap at the bilayer and multilayers is a consequence of interlayer hopping. It can be seen from Fig. 5a-d that the band extrema K_v , Γ_v and Q_c all split with the increase of the number of layers, a direct evidence of the interlayer hopping. The splitting represents the interlayer hopping strength. The splitting at Γ_v and Q_c are much larger than that at K_v . This is due to the fact that the Bloch states at K_v are predominantly from the metal d orbitals, while the Bloch states at Γ_v and Q_c have non-negligible compositions of the chalcogen p_z orbitals (*cf.* Fig. 2). The interlayer hopping integral between the p_z orbitals of the nearest neighbor chalcogen atoms is more significant compared to other orbitals. The interlayer hopping at K_v is then much weaker compared to that at Γ_v and Q_c , because the two metal planes have larger separation

compared to the two nearest neighbor chalcogen planes from the two layers. With the increase of the number of layers, the energy of Γ_v is raised and that of Q_c is lowered significantly, while the energies of K_v and Γ_v do not change much. The band gap crosses over to an indirect one at the bilayer, and further decreases with the increase of thickness.

Right at K_c , there is no visible splitting from the interlayer hopping (Fig. 5a-d). This is dictated by the rotational symmetry of the 2H bilayer lattice and the Bloch functions of each monolayer. The interlayer hopping matrix element is $H_{nn'}^{\text{int}} = \langle \psi_n^L | \hat{H}^{\text{int}} | \psi_{n'}^U \rangle$, where ψ_n^L ($\psi_{n'}^U$) is the Bloch state at the K point in the lower (upper) layer. \hat{H}^{int} is the interlayer hopping between the two layers which, in 2H stacking, is invariant under C_3 rotation (*i.e.* $C_3 \hat{H}^{\text{int}} C_3^{-1} = \hat{H}^{\text{int}}$). Thus

$$\begin{aligned} H_{nn'}^{\text{int}} &\equiv \langle \psi_n^L | C_3^{-1} C_3 \hat{H}^{\text{int}} C_3^{-1} C_3 | \psi_{n'}^U \rangle \\ &= \langle C_3 \psi_n^L | C_3 \hat{H}^{\text{int}} C_3^{-1} | C_3 \psi_{n'}^U \rangle \\ &= \langle \gamma_n^L \psi_n^L | \hat{H}^{\text{int}} | \gamma_{n'}^U \psi_{n'}^U \rangle = (\gamma_n^L)^* \times \gamma_{n'}^U H_{nn'}^{\text{int}}, \end{aligned} \quad (3)$$

in which γ_n^L and $\gamma_{n'}^U$ are the eigenvalues of the C_3 rotation for ψ_n^L and $\psi_{n'}^U$ respectively. A nonzero interlayer hopping matrix element then requires $\gamma_n^L = \gamma_{n'}^U$. Assuming that the lower layer takes the orientation in Fig. 1a, γ_n^L is directly given in Table 2, while $\gamma_{n'}^U$ is given by the complex conjugates of those in Table 2 because of the 180° rotation between the two layers that switches K and $-K$. Upon taking the rotation center to be the M site in the lower layer (the X site in the upper layer), we have $\gamma_v^L = \gamma_v^U = \omega$ for the VBs, while $\gamma_c^L = 1$ and $\gamma_c^U = \omega^*$ for the CBs. These mean that interlayer hopping is allowed between the VBM states, but is forbidden between the two CBM states at the

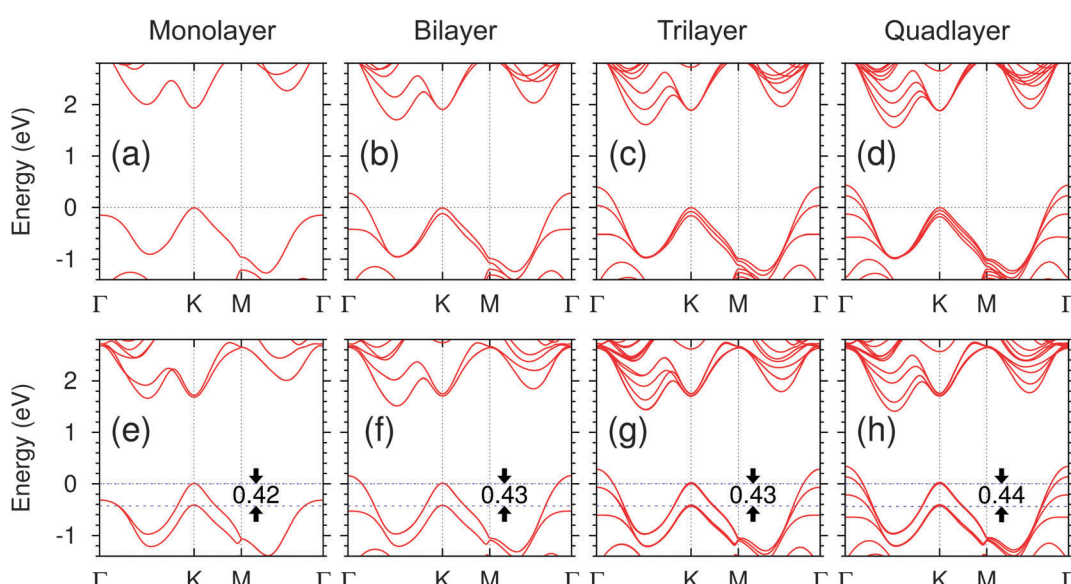


Fig. 5 First-principles band structures for WS₂ mono-, bi-, tri-, and quad-layers without SOC [(a)-(d)] and with SOC [(e)-(h)]. The valence band splittings at K point are nearly independent of the number of layers. The experimental bulk lattice constant is used in the calculations. Adapted with permission from ref. 107. Copyright 2013, Nature Publishing Group.

K point in the lower and upper layers. The strength of the VB interlayer hopping can be read out from the splitting at K_v in the absence of SOC, which is in the order of ~ 100 meV in all four TMDs.³⁴ Moreover, for the Bloch states at the *K* point with $n = n' = c + 1, v - 4$, or $v - 6$ (*cf.* Fig. 2), the identical eigenvalues under C_3 in the upper and 180° -rotated lower layers ($\gamma_n^L = \gamma_{n'}^U = \omega$, *cf.* Table 2) imply that these states have finite interlayer hoppings and hence split in 2H bilayers.

$H_{cc}^{\text{int}} = 0$ means that no interlayer hopping exists to the leading order between the K_c states in the upper and lower layers. In fact, in the absence of SOC, K_c states in the upper layer and lower layer belong to different irreducible representations of the C_3 symmetry, thus interlayer hopping vanishes to all orders between the K_c states in the two layers.[†] We note that this conclusion is unique to the 2H stacking order. A relative translation or rotation of the two layers will change the rotational symmetry of \hat{H}^{int} , allowing a finite interlayer hopping between the K_c states.

Spin-layer locking effect in $\pm K$ valleys. An interesting feature in 2H (or 2H-like) stacking is that the interlayer hopping at $\pm K$ valleys can be substantially quenched by the SOC. As shown in Fig. 5e–h for WS₂, with SOC turned on in the first-principles calculations, the band dispersions at K_v become nearly identical for mono-, bi-, tri-, and quad-layers, exhibiting only a splitting of ~ 0.43 eV which is nearly the spin-orbit splitting shown in Fig. 5e. This is due to two facts: (i) in each monolayer there is an out-of-plane spin splittings with opposite signs in the *K* and $-K$ valleys; (ii) the lower layer is an 180° rotation of the upper one in the 2H stacking. This rotation switches the two valleys in the lower layer, but leave spin unchanged (*cf.* Fig. 3a and d). Thus, the sign of the spin splitting depends on both the valley index and the layer index. Since interlayer hopping conserves both the spin and the crystal momentum, the spin splitting corresponds to an energy cost of the interlayer hopping (*cf.* Fig. 3b and e), which is larger than the hopping matrix element.^{34,35} Thus interlayer hopping is effectively quenched, especially for WX₂ where SOC is stronger. In 2H bilayers, the Bloch states in the $\pm K$ valleys are predominantly localized in either the upper or the lower layer depending on the spin, *i.e.* the spin index is locked with the layer index (*cf.* Fig. 3g and h). The *K* valley physics is essentially that of the two decoupled monolayers. The valley circular dichroism and the valley Hall effect from the two layers average out, but the spin circular dichroism and the spin Hall effect from the two layers add constructively (*cf.* Fig. 3c, f and g).³⁴ Circular polarized PL can now come from the spin circular dichroism and is not necessarily an indication of inversion symmetry breaking.^{34,35} Since the layer degree of freedom is associated with the out-of-plane electric polarization, while spin couples to

magnetic field, the spin-layer locking also leads to a variety of interesting magnetoelectric effects.^{33,34,177}

Heterostructures of different TMDs. Manually assembled (stacked) monolayers can lead to a variety of vertical heterostructures between different group-VIB TMDs^{132,145,178–181} and between TMDs and other 2D crystals,^{4,182} which are of interest because they make possible semiconductor heterojunctions in the 2D limit.

First-principles calculations have studied various lattice matching heterostructures of either the AB stacking (the M/X site of one layer right on top of the X/M site of the other) or the AA stacking (the M/X site of one layer right on top of the M/X site of the other). These heterobilayers have the same hexagonal BZ as the monolayers. Unlike TMD homobilayers which all have indirect band gaps, calculations show that some of these lattice matching heterobilayers exhibit direct band gaps at the *K* points. For example, MoS₂–WSe₂ and WS₂–WSe₂ heterobilayers are found to be direct band gap semiconductors in the various first-principles calculations reported.^{113,183,184} The MoS₂–WS₂ heterobilayer is reported to have an indirect band gap^{113,183–185} or a direct band gap¹⁴¹ depending on the interlayer distance adopted in the calculations. Like the homobilayers, computational details, such as van der Waals corrections, SOC, GW corrections, matched lattice constant with strain, *etc.*, may give some different details of the band structures of the heterobilayers.^{141,184–186}

An interesting observation from these first-principles calculations of heterobilayers is that the CB and VB states at the *K* points are predominantly localized in an individual layer. In particular, they exhibit the type-II band-edge alignment with the CBM and VBM residing in opposite layers.^{113,141,184,185,187} Such type-II heterojunctions result from the workfunction and band gap differences between the TMDs. The resultant conduction band offset (CBO) and valence band offset (VBO) between the monolayers are found to be a few hundred meV from these calculations. Note that the CBO and VBO correspond to the energy cost of interlayer hopping, hence the large CBO and VBO will substantially quench the hybridization between the layers, making the band structures of the heterobilayers almost the superposition of that of the constituent monolayers.^{132,141,185}

According to the measured bulk lattice constants: 3.160 Å for MoS₂,¹⁸⁸ 3.153 Å for WS₂,¹⁸⁹ 3.288 Å for MoSe₂,¹⁸⁸ and 3.282 Å for WSe₂,¹⁸⁹ lattice matching heterobilayers are more likely to form between MoS₂ and WS₂, and between MoSe₂ and WSe₂. For other combinations with large mismatch in the lattice constants, first-principles calculations have found that the interlayer couplings (van der Waals interactions) are not strong enough to make the two layers match their lattices.¹⁸⁷ The manually assembled TMD heterostructures in general lead to misalignment between the layers.

For the manually stacked TMD bilayer heterostructures, optical studies have shown the spectral features of both the intralayer exciton with electron and hole from the same layer and the interlayer exciton with electron and hole from the different layers.^{145,178–181} For example, in the MoSe₂–WSe₂

[†] We note that small yet finite (\sim meV) interlayer splitting exists for the K_c states calculated by the VASP software. This splitting is confirmed to be artificial due to the numerical errors introduced by VASP. TMD bilayers calculated by a more accurate software, *i.e.* WIEN2k, show no splitting for the K_c state, which is consistent with the symmetry analysis.

heterostructures,¹⁴⁵ neutral and charged intralayer excitons from both the MoSe₂ layer and WSe₂ layer can be clearly identified in the PL spectral from the heterojunction region, and they have identical energies to the ones in isolated MoSe₂ monolayer and WSe₂ monolayer. These further confirm that hybridization between the layers is small for the band edge states. The interlayer exciton is found to have an energy a few hundred meV below the intralayer one, consistent with the type-II band edge alignment and the magnitude of CBO and VBO from the first-principles calculations.

For MoS₂-WS₂ and MoS₂-WSe₂ heterostructures, the VBO and CBO have also been directly measured by micro-beam X-ray photoelectron spectroscopy (XPS) and STS.¹³² For MoS₂-WSe₂ heterostructure, the VBO is directly measured to be 0.41 eV by the XPS. This VBO can also be inferred from STS measurements of MoS₂ and WSe₂ monolayers both on graphite, where the deduced VBO is 0.36 eV, consistent with XPS result. And the deduced value for CBO between MoS₂-WSe₂ is 0.52 eV from STS and 0.57 eV combining the VBO from XPS and the band gap measured from STS. The CBM is found to reside in the MoS₂ layer and VBM in the WSe₂ layer. MoS₂-WS₂ heterostructure is shown to be a similar type-II heterojunction with a smaller VBO of 0.23 eV measured using XPS, and a deduced CBO of ~0.4 eV. WS₂-WSe₂ heterostructure is also shown to be a type-II heterojunction with CBM in the WS₂ layer and VBM in the WSe₂ layer, while both CBO and VBO are ~0.2 eV.¹³²

In these type-II heterostructures, the observation of interlayer exciton in the PL spectrum shows that there is residue hybridization between the layers, such that CBM electrons still have a finite albeit small spatial overlap with the VBM holes residing largely in the opposite layer. The interlayer exciton is therefore still optically bright, but has much smaller optical dipole compared to the intralayer exciton. This gives rise to long recombination lifetime measured for interlayer exciton which exceeds ns,¹⁴⁵ orders of magnitude longer than the intralayer ones. With electron and hole constitutions in opposite layers, interlayer excitons correspond to a permanent electric dipole in the out-of-plane direction, evidenced from the gate dependence of its resonance energy.¹⁴⁵ Repulsive interactions between these dipole-aligned interlayer excitons are also inferred from the excitation power dependence of the PL spectra. With the observed ultralong lifetime and the repulsive interaction,¹⁴⁵ the interlayer exciton in TMD heterostructures may provide an ideal system to explore the exotic phenomenon of excitonic condensation,¹⁹⁰ as well as optoelectronic applications such as the excitonic circuit and heterostructure lasers. Such interlayer excitons will also form the basis for optical control of layer degree of freedom in van der Waals layered structures.

3 Theoretical models

Theoretical models have been developed at different levels to describe the complex electronic structures of TMD monolayers, including both *k*-*p* models^{23,100,125,191} and TB models.^{100,118,142,173,191} Among the various models, the simplest and widely used one is the

two-band *k*-*p* model describing the neighborhood of the ±*K* points²³

$$H_{k,p} = at(\tau k_x \sigma_x + k_y \sigma_y) + \frac{\Delta}{2} \sigma_z - \lambda_v \tau s_z \frac{\sigma_z - 1}{2}$$

$$= \begin{bmatrix} \Delta/2 & at(\tau k_x - ik_y) \\ at(\tau k_x + ik_y) & -\Delta/2 + \lambda_v \tau s_z \end{bmatrix}, \quad (4)$$

in which $\sigma_{x/y/z}$ is the Pauli matrix spanning the conduction and valence states at ±*K* points, which are formed respectively by the d₀ and d_{2τ} orbitals respectively. $\tau = \pm 1$ is the valley index, and $s_z = \pm 1$ is the spin index. a is the lattice constant, and $k_{x/y}$ is the wave vector measured from ±*K*. The effective hopping integral t , the band gap Δ , and the SOC splitting $2\lambda_v$ in the VB can all be fitted from the first-principles band structures in the neighborhood of *K* points. Interestingly, this two-band *k*-*p* model is in fact the massive Dirac fermion model. This simple model explains why the electron and hole masses are comparable, since they are largely acquired from the mutual coupling of the two bands. It also well captures the low-energy band-edge physics in the ±*K* valleys, including the band dispersion, the giant SOC splitting of the VB, the valley dependent Berry curvature and orbital magnetic moment, and the valley dependent optical selection rule.²³ Table 6 is a comparison of the Berry curvatures from this model and from first-principles calculations for the four monolayer TMDs, which shows remarkable agreement.

The SOC in this two-band *k*-*p* model is from the intra-atomic contribution $L \cdot S$, thus it vanishes for the CB, missing the two origins of the small CB splitting: the second-order coupling with remote M-d_{±1} orbitals; and the first-order effect from the minor X-p_{±1} compositions.^{100,115,125,144} Nevertheless, the CB spin splitting has to take the same symmetry-dictated form as the VB one as discussed earlier.³⁵ This valley dependent spin splitting term $\lambda_v \tau s_z$ can be phenomenologically added to the CB edge for correction.^{72,144,192}

The two-band *k*-*p* model has been widely used to study various properties of TMD monolayers because of its simplicity.^{135,192–206} In the meantime, the simplicity of this model inevitably imposes some limitations on its applications. For example, it can not account for the electron-hole asymmetry and the trigonal warping of band dispersion. The two limitations can be overcome by introducing terms quadratic in k ^{100,191} or cubic in k .^{100,125} The corrected models with high-order terms have been used to study optical conductivity,²⁰⁷ magneto-optical properties,¹⁹² plasmons,²⁰⁸ and spin relaxation.²⁰⁹ Apart from the most studied ±*K* valley, the *I* valley of VB can be well described by an effective-mass model nearly unaffected by SOC.¹²⁵ For the *Q* valleys of CB, there lacks simple models because of its low symmetry.

While the *k*-*p* approximation aims to describe the electronic structures only in the neighborhood of a critical point of high symmetry in the momentum space, TB models can in principle reproduce the band dispersions in the entire BZ, suitable for studying edge states, finite size systems such as quantum dots, as well as for calculating mesoscopic transport. TB models have been constructed for TMD monolayers in various approximation

levels, with different number of bands (or the number of orbitals in a unit cell) involved and different cut-off distances of hoppings. There are (i) 7-band and 5-band TB models,¹⁹¹ (ii) 27-band TB model,¹⁷³ (iii) 11-band TB model,^{118,142} and (iv) 3-band TB model.¹⁰⁰ Here the number of bands is counted in the spinless case, and the actual number of bands doubles when SOC is added to the model.

(i) The 7-band TB model¹⁹¹ contains three Mo-d orbitals ($\text{Mo-d}_0, \text{d}_{\pm 2}$), four S-p orbitals (upper and lower $\text{S-p}_{\pm 1}$), only Mo-S nearest-neighbor (NN) hoppings, and overlap integrals. The hopping integrals are in the Slater-Koster (SK) two-center approximation.²¹⁰ Then the model is reduced to a 5-band model whose basis states all have even symmetry under σ_h . The model can describe the lowest CB and the top VB in the $\pm K$ valleys, while there is large discrepancy over the rest k -space region.¹⁹¹ Another limitation is that it does not reproduce correctly the order in energy of other conduction and valence bands. This model has been used to derive the two-band $k\cdot p$ model with quadratic terms by expansion at $\pm K$ followed by reduction to the two bands in the Löwdin partitioning method.^{211,212}

(ii) The 27-band TB model¹⁷³ contains the complete set of sp^3d^5 orbitals of the metal atom and the two chalcogen atoms. The model considers NN SK hoppings of M-M, M-X, and X-X as well as the corresponding overlap integrals. The total number of parameters of the model is 96. It well reproduces all bands from the first-principles bands (in energy range of $-3\text{--}3$ eV) in the entire BZ. Moreover, this model can apply to monolayer, bulk, and bilayer using the same set of parameters, all in good agreement with the first-principles bands. This model is suitable for numerical studies in need of accurate band descriptions in the entire BZ, but can be too complicated for many studies.

(iii) The 11-band TB model¹¹⁸ contains five M-d orbitals and three p orbitals for each of the two X atoms. This model also considers NN SK hoppings of M-M, M-X, and X-X like the 27-band model, while this model uses orthogonal bases and hence does not need overlap integrals. When SOC is not considered, the 11-band model can be divided into decoupled 6×6 block and 5×5 block which consist of even and odd parity states respectively under the σ_h operation. This model is relatively complete in orbitals for the generally concerned 11 bands (4 above and 7 below the band gap) and keeps its relative simplicity compared to the 27-band model. Because both the VB and CB are σ_h -even, only the parameters for the σ_h -even 6×6 block are fitted.¹¹⁸ The fitted bands agree qualitative well with the first-principles band structures, but the quantitative discrepancy can be large away from the K and Γ points. With interlayer X-X hoppings considered, this model can be used to qualitatively explain the direct-to-indirect band gap transition from monolayer to bulk. SOC interactions have been added to the latest development of this 11-band model to make it more realistic.¹⁴²

(iv) The 3-band TB model¹⁰⁰ is constructed with the three M-d orbitals only, *i.e.* d_{z^2} , d_{xy} , and $\text{d}_{x^2-y^2}$. Symmetry-based non-SK M-M hoppings of both NN interactions and up to the third-nearest-neighbor (TNN) interactions are considered in this model. Orthogonal bases are used so that overlap integrals are not needed. Fitting parameters are given for all MX_2 monolayers in this model. The bands from the NN TB model

agree well with the first-principles ones only for the VB and CB in the $\pm K$ valleys (*cf.* Fig. 6a and c), while the bands from the TNN TB model agree well with the first-principles ones in the entire BZ due to the introduction of more hoppings (*cf.* Fig. 6b and d). With the absence of X-p orbitals in the model, physical quantities such as Berry curvature which rely on the wavefunction structure can be described well only in k -space regions where M-d orbital dominates over the X-p orbitals (*e.g.* VB and CB in $\pm K$ valleys) for both the NN TB and TNN TB models. The SOC splitting of VB can also be well described. Due to the simplicity of this model, it can be particularly useful in the study of many-body physics and finite size systems. This model has been applied to the study of edge states in MX_2 nanoribbons,⁷⁰ quantum dots formed by lateral confinement potential in the extended MX_2 monolayer,⁷³ intercellular orbital magnetic moment,³¹ magnetoelectronic and optical properties,²¹³ and magnetoluminescence.²¹⁴

All the TB models introduced above are capable of describing the low-energy physics of monolayer TMDs in the $\pm K$ valleys. The 3-band TNN TB model is the simplest model that gives a reasonably good description of the top VB and lowest CB in the entire BZ. In order to capture features such as the CB splitting, $\text{M-d}_{xz}, \text{d}_{yz}$ and $\text{X-p}_x, \text{p}_y$ orbitals have to be included, as in the 11-band and 27-band models, which complicates the models inevitably. The TB models in (i)–(iii) are all based on the SK two-center approximation, while the 3-band TB model in (iv) is not SK-like but fully based on the symmetry. SK hoppings omit all contributions from three-center integrals, while symmetry-based non-SK hoppings include three-center integrals and make no approximations. This difference can be crucial. For example, besides 2 onsite energies, the 3-band NN TB model has 6 hoppings. However, if the 3-band model is constructed in the SK approximation, there are only 3 hoppings, namely V_{ddg} , V_{ddr} , and $V_{dd\delta}$. The agreement between the TB bands and first-principles bands can always be improved by having more fitting parameters, either by introducing more orbitals or by introducing more hopping integrals. The success of the 3-band model with the relative simplicity suggests that going beyond the SK framework can be a viable way of improving the accuracy of the models.

By introducing interlayer hoppings, all the TB models for the monolayer can be extended to describe bilayer and multilayer homostructures. Interlayer hoppings are explicitly included in both the 27-band and the 11-band TB models to describe bilayer or bulk. In general, the X-p_z orbital should be included in a TB model to describe the interlayer interactions reliably, since it plays a crucial role in the interlayer hopping over a large range of the BZ, *e.g.* at Γ_v and Q_c . However, if only the physics in $\pm K$ valleys are of interest, effective interlayer hoppings can also be included in models constructed with M-d orbitals.

For 2H bilayers, a four-band $k\cdot p$ model has been derived based on the 3-band TB model of monolayers,^{33,34}

$$H(\mathbf{k}) = \begin{bmatrix} \Delta & atk_+^\tau & 0 & 0 \\ atk_-^\tau & -\tau_z s_z \lambda_v & 0 & t_\perp \\ 0 & 0 & \Delta & atk_-^\tau \\ 0 & t_\perp & atk_+^\tau & \tau_z s_z \lambda_v \end{bmatrix} \quad (5)$$

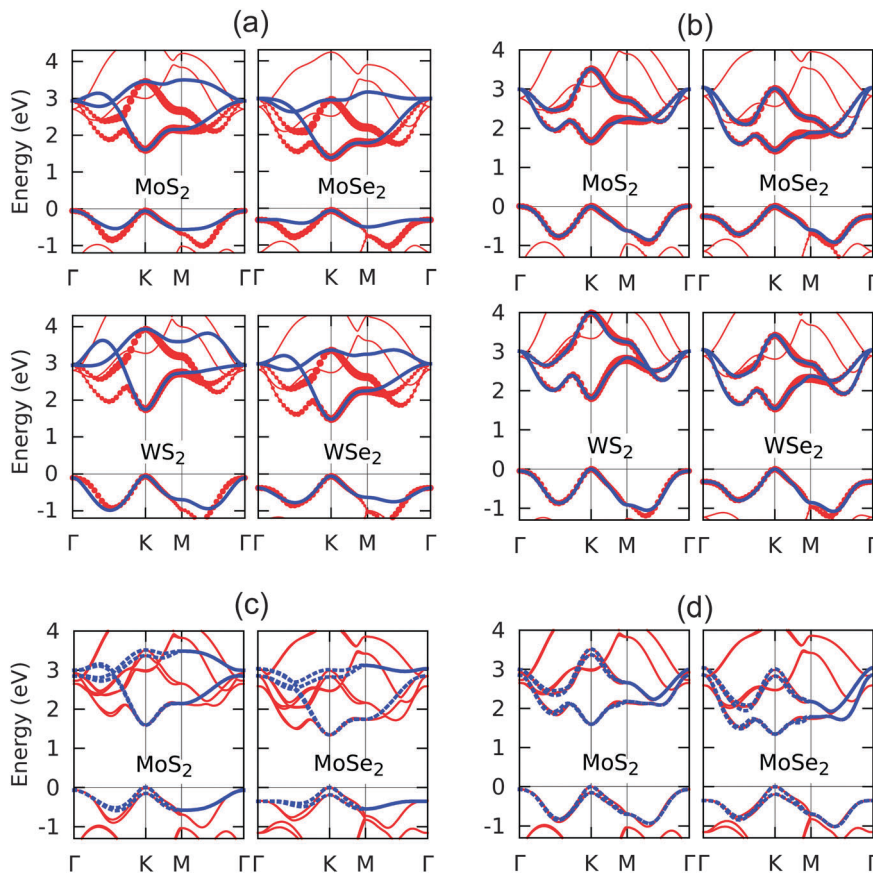


Fig. 6 Comparison between the bands from the 3-band TB model (blue curves) and the first-principles ones (red curves and dots) for TMD monolayers. (a) Bands from NN TB without SOC. (b) Bands from TNN TB without SOC. Red dots in (a) and (b) show the compositions from the d_{z^2} , d_{xy} , and $d_{x^2-y^2}$ orbitals. (c) Bands from NN TB with SOC. (d) Bands from TNN TB with SOC. Adapted with permission from ref. 100. Copyright 2013, American Physical Society.

in which $k_\pm^\tau = \tau_z k_x \pm i k_y$. In this model, only the k -independent leading order term is retained for the interlayer hopping matrix element. The interlayer hopping exists only between the VB K_v states in the two layers, while it vanishes between the CB states at K_c due to the symmetry (see discussion in Section 2.2). The magnitude $2t_\perp$ can be extracted from the VB splitting at K from the first-principles calculations of the bilayer band structures in the absence of SOC. CB SOC and interlayer bias can be phenomenologically added to this model. This Hamiltonian has been used to describe the tunable valley optical circular dichroism and orbital magnetic moment as a function of interlayer bias,³³ as well as the magnetoelectric effects in the 2H stacked bilayers.^{34,35}

In the very proximity of K_v , the above bilayer Hamiltonian simply reduces to:

$$H_K = \lambda_v \tau s_z \zeta_z + t_\perp \zeta_x, \quad (6)$$

where $\zeta_{z,x}$ is the Pauli matrix for the layer pseudospin: $\zeta_z = 1$ for upper layer and $\zeta_z = -1$ for lower layer. τ and s_z are respectively the valley pseudospin and the real spin.^{34,35} The SOC term corresponds to the spin splitting in the out-of-plane direction with a valley and layer dependent sign in the 2H bilayer, as discussed in Section 2.2. It manifests as an effective coupling

between the spin, valley pseudospin and the layer pseudospin in bilayer. $t_\perp \zeta_x$ is the interlayer hopping term that conserves the spin and the crystal momentum. The competition of the SOC term and the interlayer hopping term determines the small hybridization between the two layers in the proximity of K_v . The energy eigenstates are associated with a spin- and valley-dependent layer polarization $\langle \zeta_z \rangle = -\tau s_z \frac{\lambda_v}{\sqrt{\lambda_v^2 + t_\perp^2}}$, which are found in excellent agreement with the first-principles wavefunctions.³⁴ The interlayer hopping and hence layer hybridization at K_c vanishes due to symmetry. This difference in the layer hybridization at K_c and K_v can result in their different energy shifts in a perpendicular electric field, which has explained the observed splitting of the interlayer and intralayer trion resonances as a function of interlayer bias in the PL measurement.³⁵

4 Conclusions

In this review article, we provide an overview of the current understanding of the various aspects of the electronic structures in 2D group-VIB TMDs and the theoretical models developed for describing the essential features. Apart from the two-dimensionality and the visible-frequency-range direct band

gap at the monolayer limit, these 2D semiconductors are distinguished from all existing systems by their extraordinary properties including the valley pseudospin of band edge carriers, the valley dependent Berry phase related properties, the ultra-strong spin-orbit coupling that leads to the strong interplay between spin and various pseudospins, and the strong Coulomb interaction evidenced from the exceptionally large excitonic effects. These imply varieties of interesting opportunities for the exploration of device applications as well as fundamental new physics. Although the electronic structures are complex in general with the involvement of multiple d orbitals of the metal atom and p orbitals of the chalcogen atom, the band edge physics in $\pm K$ valleys which is of most interest for transport and optical studies is well understood with a remarkably simple model that makes a good example of massive Dirac fermions in the limit of large gap opening.

We note that this review article has a limited scope, focusing only on the single particle electronic structures of the 2D bulk. This is partially due to the lack of understanding of the many-body effects,²¹⁵ and the electronic structures on the edges, grain boundaries, and impurities. Even for the 2D bulk, several aspects of the electronic structures still remain unclear and need further experimental and theoretical studies to clarify, and we mention a few here. An outstanding issue of most importance is to determine the difference between the electronic and optical band gaps, *i.e.* the exciton binding energy. First-principles calculations and various experimental studies using STS, ARPES, optical spectroscopies have agreed on the order of magnitude of this quantity, while quantitative agreement is yet to be achieved. The accurate experimental determination of the exciton binding energy and the exciton excited state are also essential in understanding the screened Coulomb interaction in these 2D semiconductors.^{39,46} The energies of the Q_c and Γ_v valleys relative to the CBM and VBM in monolayers remain unclear. These quantities can be crucial in the study of inter-valley relaxation of band edge carriers which is likely to be mediated by these valleys close by in energy. The energies of Q_c and Γ_v from first-principles calculations are various due to the choice of approximations and the lack of accurate information on lattice constant. The same problem has also led to the conflicting conclusions on the indirect band gap and VBM and CBM in bilayers from the first-principles calculations. ARPES and STS can provide powerful approaches to determine the energies of these valleys.^{18,45,46}

A lot of recent experimental efforts have been placed on the study of heterostructures between different 2D TMDs,^{132,145,178–181} which may lead to even richer possibilities for new physics and device applications. The understanding of the interlayer hopping process is indispensable in the exploration of the new properties of the heterostructures. First-principles calculations of AB and AA stacked heterostructures have suggested that the hybridization between the layers is weak, due to the large band offsets revealed from STS and XPS,¹³² and PL measurement.^{145,178–181} The order of magnitude of the hopping matrix element is of importance in determining the optical dipole moment of interlayer exciton, and its dependence on the twisting angle between the layers is of

interest. First-principles calculations can only address very limited cases of the heterostructures, and efficient theoretical models are needed with input from the first-principles calculations.

Acknowledgements

WY acknowledges support from the Croucher Foundation under the Croucher Innovation Award, and the RGC (HKU705513P, HKU9/CRF/13G) and UGC (AoE/P-04/08) of Hong Kong SAR. GBL acknowledges support from the NSFC with Grant No. 11304014, the National Basic Research Program of China 973 Program with Grant No. 2013CB934500 and the Basic Research Funds of Beijing Institute of Technology with Grant No. 20131842001 and 20121842003. DX acknowledges support from the National Science Foundation, Office of Emerging Frontiers in Research and Innovation (EFRI – 1433496). YY acknowledges support from the MOST Project of China with Grants No. 2014CB920903 and 2011CBA00100, the NSFC with Grant No. 11174337 and 11225418, the Specialized Research Fund for the Doctoral Program of Higher Education of China with Grants No. 20121101110046. XX acknowledges support from DoE, BES, Materials Science and Engineering Division (DE-SC0008145), the National Science Foundation (DMR-1150719), and the National Science Foundation, Office of Emerging Frontiers in Research and Innovation (EFRI – 1433496).

References

- 1 K. S. Novoselov, D. Jiang, F. Schedin, T. J. Booth, V. V. Khotkevich, S. V. Morozov and A. K. Geim, *Proc. Natl. Acad. Sci. U. S. A.*, 2005, **102**, 10451–10453, DOI: 10.1073/pnas.0502848102.
- 2 Z. Zeng, Z. Yin, X. Huang, H. Li, Q. He, G. Lu, F. Boey and H. Zhang, *Angew. Chem., Int. Ed.*, 2011, **50**, 11093–11097, DOI: 10.1002/anie.201106004.
- 3 J. N. Coleman, M. Lotya, A. O'Neill, S. D. Bergin, P. J. King, U. Khan, K. Young, A. Gaucher, S. De, R. J. Smith, I. V. Shvets, S. K. Arora, G. Stanton, H.-Y. Kim, K. Lee, G. T. Kim, G. S. Duesberg, T. Hallam, J. J. Boland, J. J. Wang, J. F. Donegan, J. C. Grunlan, G. Moriarty, A. Shmeliov, R. J. Nicholls, J. M. Perkins, E. M. Grieveson, K. Theuwissen, D. W. McComb, P. D. Nellist and V. Nicolosi, *Science*, 2011, **331**, 568–571, DOI: 10.1126/science.1194975.
- 4 A. K. Geim and I. V. Grigorieva, *Nature*, 2013, **499**, 419–425, DOI: 10.1038/nature12385.
- 5 S. Lebègue and O. Eriksson, *Phys. Rev. B: Condens. Matter Mater. Phys.*, 2009, **79**, 115409, DOI: 10.1103/PhysRevB.79.115409.
- 6 Y. Ding, Y. Wang, J. Ni, L. Shi, S. Shi and W. Tang, *Phys. B*, 2011, **406**, 2254–2260, DOI: 10.1016/j.physb.2011.03.044.
- 7 W. G. Dawson and D. W. Bullett, *J. Phys. C: Solid State Phys.*, 1987, **20**, 6159.
- 8 J. Augustin, V. Eyert, T. Böker, W. Frentrup, H. Dwelk, C. Janowitz and R. Manzke, *Phys. Rev. B: Condens. Matter Mater. Phys.*, 2000, **62**, 10812.
- 9 S. Tongay, H. Sahin, C. Ko, A. Luce, W. Fan, K. Liu, J. Zhou, Y.-S. Huang, C.-H. Ho, J. Yan, D. F. Ogletree, S. Aloni, J. Ji,

- S. Li, J. Li, F. M. Peeters and J. Wu, *Nat. Commun.*, 2014, **5**, 3252, DOI: 10.1038/ncomms4252.
- 10 T. Böker, R. Severin, A. Müller, C. Janowitz, R. Manzke, D. Vo, P. Krüger, A. Mazur and J. Pollmann, *Phys. Rev. B: Condens. Matter Mater. Phys.*, 2001, **64**, 235305, DOI: 10.1103/PhysRevB.64.235305.
- 11 A. Splendiani, L. Sun, Y. Zhang, T. Li, J. Kim, C.-Y. Chim, G. Galli and F. Wang, *Nano Lett.*, 2010, **10**, 1271–1275, DOI: 10.1021/nl903868w.
- 12 K. F. Mak, C. Lee, J. Hone, J. Shan and T. F. Heinz, *Phys. Rev. Lett.*, 2010, **105**, 136805, DOI: 10.1103/PhysRevLett.105.136805.
- 13 B. Radisavljevic, A. Radenovic, J. Brivio, V. Giacometti and A. Kis, *Nat. Nanotechnol.*, 2011, **6**, 147–150, DOI: 10.1038/nnano.2010.279.
- 14 K.-K. Liu, W. Zhang, Y.-H. Lee, Y.-C. Lin, M.-T. Chang, C.-Y. Su, C.-S. Chang, H. Li, Y. Shi, H. Zhang, C.-S. Lai and L.-J. Li, *Nano Lett.*, 2012, **12**, 1538–1544, DOI: 10.1021/nl2043612.
- 15 Y. Zhan, Z. Liu, S. Najmaei, P. M. Ajayan and J. Lou, *Small*, 2012, **8**, 966–971, DOI: 10.1002/smll.201102654.
- 16 A. M. van der Zande, P. Y. Huang, D. A. Chenet, T. C. Berkelbach, Y. You, G.-H. Lee, T. F. Heinz, D. R. Reichman, D. A. Muller and J. C. Hone, *Nat. Mater.*, 2013, **12**, 554–561, DOI: 10.1038/nmat3633.
- 17 S. Najmaei, Z. Liu, W. Zhou, X. Zou, G. Shi, S. Lei, B. I. Yakobson, J.-C. Idrobo, P. M. Ajayan and J. Lou, *Nat. Mater.*, 2013, **12**, 754–759, DOI: 10.1038/nmat3673.
- 18 Y. Zhang, T.-R. Chang, B. Zhou, Y.-T. Cui, H. Yan, Z. Liu, F. Schmitt, J. Lee, R. Moore, Y. Chen, H. Lin, H.-T. Jeng, S.-K. Mo, Z. Hussain, A. Bansil and Z.-X. Shen, *Nat. Nanotechnol.*, 2014, **9**, 111–115, DOI: 10.1038/nnano.2013.277.
- 19 H. Liu, L. Jiao, F. Yang, Y. Cai, X. Wu, W. Ho, C. Gao, J. Jia, N. Wang and H. Fan, *et al.*, *Phys. Rev. Lett.*, 2014, **113**, 066105, DOI: 10.1103/physrevlett.113.066105.
- 20 Q. H. Wang, K. Kalantar-Zadeh, A. Kis, J. N. Coleman and M. S. Strano, *Nat. Nanotechnol.*, 2012, **7**, 699–712, DOI: 10.1038/nnano.2012.193.
- 21 X. Xu, W. Yao, D. Xiao and T. F. Heinz, *Nat. Phys.*, 2014, **10**, 343–350, DOI: 10.1038/nphys2942.
- 22 W. Yao, D. Xiao and Q. Niu, *Phys. Rev. B: Condens. Matter Mater. Phys.*, 2008, **77**, 235406, DOI: 10.1103/PhysRevB.77.235406.
- 23 D. Xiao, G.-B. Liu, W. Feng, X. Xu and W. Yao, *Phys. Rev. Lett.*, 2012, **108**, 196802, DOI: 10.1103/PhysRevLett.108.196802.
- 24 H. Zeng, J. Dai, W. Yao, D. Xiao and X. Cui, *Nat. Nanotechnol.*, 2012, **7**, 490–493, DOI: 10.1038/nnano.2012.95.
- 25 T. Cao, G. Wang, W. Han, H. Ye, C. Zhu, J. Shi, Q. Niu, P. Tan, E. Wang, B. Liu and J. Feng, *Nat. Commun.*, 2012, **3**, 887, DOI: 10.1038/ncomms1882.
- 26 K. F. Mak, K. He, J. Shan and T. F. Heinz, *Nat. Nanotechnol.*, 2012, **7**, 494–498, DOI: 10.1038/nnano.2012.96.
- 27 A. M. Jones, H. Yu, N. J. Ghimire, S. Wu, G. Aivazian, J. S. Ross, B. Zhao, J. Yan, D. G. Mandrus, D. Xiao, W. Yao and X. Xu, *Nat. Nanotechnol.*, 2013, **8**, 634, DOI: 10.1038/nnano.2013.151.
- 28 D. Xiao, W. Yao and Q. Niu, *Phys. Rev. Lett.*, 2007, **99**, 236809, DOI: 10.1103/PhysRevLett.99.236809.
- 29 K. F. Mak, K. L. McGill, J. Park and P. L. McEuen, *Science*, 2014, **344**, 1489–1492, DOI: 10.1126/science.1250140.
- 30 G. Aivazian, Z. Gong, A. M. Jones, R.-L. Chu, J. Yan, D. G. Mandrus, C. Zhang, D. Cobden, W. Yao, X. Xu, 2014, arXiv: 1407.2645.
- 31 A. Srivastava, M. Sidler, A. V. Allain, D. S. Lembke, A. Kis, A. Imamoglu, 2014, arXiv:1407.2624.
- 32 D. MacNeill, C. Heikes, K. F. Mak, Z. Anderson, A. Kormányos, V. Zólyomi, J. Park, D. C. Ralph, 2014, arXiv:1407.0686.
- 33 S. Wu, J. S. Ross, G.-B. Liu, G. Aivazian, A. Jones, Z. Fei, W. Zhu, D. Xiao, W. Yao, D. Cobden and X. Xu, *Nat. Phys.*, 2013, **9**, 149–153, DOI: 10.1038/nphys2524.
- 34 Z. Gong, G.-B. Liu, H. Yu, D. Xiao, X. Cui, X. Xu and W. Yao, *Nat. Commun.*, 2013, **4**, 2053, DOI: 10.1038/ncomms3053.
- 35 A. M. Jones, H. Yu, J. S. Ross, P. Klement, N. J. Ghimire, J. Yan, D. G. Mandrus, W. Yao and X. Xu, *Nat. Phys.*, 2014, **10**, 130–134, DOI: 10.1038/nphys2848.
- 36 K. F. Mak, K. He, C. Lee, G. H. Lee, J. Hone, T. F. Heinz and J. Shan, *Nat. Mater.*, 2013, **12**, 207–211, DOI: 10.1038/nmat3505.
- 37 J. S. Ross, S. Wu, H. Yu, N. J. Ghimire, A. M. Jones, G. Aivazian, J. Yan, D. G. Mandrus, D. Xiao, W. Yao and X. Xu, *Nat. Commun.*, 2013, **4**, 1474, DOI: 10.1038/ncomms2498.
- 38 J. Feng, X. Qian, C.-W. Huang and J. Li, *Nat. Photonics*, 2012, **6**, 866–872, DOI: 10.1038/nphoton.2012.285.
- 39 D. Y. Qiu, F. H. da Jornada and S. G. Louie, *Phys. Rev. Lett.*, 2013, **111**, 216805, DOI: 10.1103/physrevlett.111.216805.
- 40 A. Chernikov, T. C. Berkelbach, H. M. Hill, A. Rigosi, Y. Li, O. B. Aslan, D. R. Reichman, M. S. Hybertsen, T. F. Heinz, 2014, arXiv:1403.4270.
- 41 K. He, N. Kumar, L. Zhao, Z. Wang, K. F. Mak, H. Zhao, J. Shan, 2014, arXiv:1406.3095.
- 42 Z. Ye, T. Cao, K. O'Brien, H. Zhu, X. Yin, Y. Wang, S. G. Louie and X. Zhang, *Nature*, 2014, **513**, 214–218, DOI: 10.1038/nature13734.
- 43 B. Zhu, X. Chen, X. Cui, 2014, arXiv:1403.5108.
- 44 G. Wang, X. Marie, I. Gerber, T. Amand, D. Lagarde, L. Bouet, M. Vidal, A. Balocchi, B. Urbaszek, 2014, arXiv:1404.0056.
- 45 C. Zhang, A. Johnson, C.-L. Hsu, L.-J. Li and C.-K. Shih, *Nano Lett.*, 2014, **14**, 2443–2447, DOI: 10.1021/nl501133c.
- 46 M. M. Ugeda, A. J. Bradley, S.-F. Shi, F. H. da Jornada, Y. Zhang, D. Y. Qiu, S.-K. Mo, Z. Hussain, Z.-X. Shen, F. Wang, S. G. Louie, M. F. Crommie, 2014, arXiv:1404.2331.
- 47 H. Fang, S. Chuang, T. C. Chang, K. Takei, T. Takahashi and A. Javey, *Nano Lett.*, 2012, **12**, 3788–3792, DOI: 10.1021/nl301702r.
- 48 W. Liu, J. Kang, D. Sarkar, Y. Khatami, D. Jena and K. Banerjee, *Nano Lett.*, 2013, **13**, 1983–1990, DOI: 10.1021/nl304777e.
- 49 B. W. H. Baugher, H. O. H. Churchill, Y. Yang and P. Jarillo-Herrero, *Nano Lett.*, 2013, **13**, 4212–4216, DOI: 10.1021/nl401916s.
- 50 B. Radisavljevic and A. Kis, *Nat. Mater.*, 2013, **12**, 815–820, DOI: 10.1038/nmat3687.
- 51 H. S. Lee, S. S. Baik, S.-W. Min, P. J. Jeon, J. S. Kim, K. Choi, S. Ryu, H. J. Choi, J. H. Kim, S. Im, 2014, arXiv:1406.6779.
- 52 A. Pospischil, M. M. Furchi and T. Mueller, *Nat. Nanotechnol.*, 2014, **9**, 257–261, DOI: 10.1038/nnano.2014.14.

- 53 B. W. H. Baugher, H. O. H. Churchill, Y. Yang and P. Jarillo-Herrero, *Nat. Nanotechnol.*, 2014, **9**, 262–267, DOI: 10.1038/nnano.2014.25.
- 54 J. S. Ross, P. Klement, A. M. Jones, N. J. Ghimire, J. Yan, D. G. Mandrus, T. Taniguchi, K. Watanabe, K. Kitamura, W. Yao, D. H. Cobden and X. Xu, *Nat. Nanotechnol.*, 2014, **9**, 268–272, DOI: 10.1038/nnano.2014.26.
- 55 Y. J. Zhang, T. Oka, R. Suzuki, J. T. Ye and Y. Iwasa, *Science*, 2014, **344**, 725–728, DOI: 10.1126/science.1251329.
- 56 H. Yu, Y. Wu, G.-B. Liu, X. Xu and W. Yao, *Phys. Rev. Lett.*, 2014, **113**, 156603, DOI: 10.1103/PhysRevLett.113.156603.
- 57 S. Helveg, J. Lauritsen, E. Lægsgaard, I. Stensgaard, J. Nørskov, B. Clausen, H. Topsøe and F. Besenbacher, *Phys. Rev. Lett.*, 2000, **84**, 951–954, DOI: 10.1103/physrevlett.84.951.
- 58 M. Bollinger, J. Lauritsen, K. Jacobsen, J. Nørskov, S. Helveg and F. Besenbacher, *Phys. Rev. Lett.*, 2001, **87**, 196803, DOI: 10.1103/PhysRevLett.87.196803.
- 59 Y. Li, Z. Zhou, S. Zhang and Z. Chen, *J. Am. Chem. Soc.*, 2008, **130**, 16739–16744, DOI: 10.1021/ja805545x.
- 60 A. R. Botello-Méndez, F. López-Urías, M. Terrones and H. Terrones, *Nanotechnology*, 2009, **20**, 325703, DOI: 10.1088/0957-4484/20/32/325703.
- 61 C. Ataca, H. Åzahin, E. Aktürk and S. Ciraci, *J. Phys. Chem. C*, 2011, **115**, 3934–3941, DOI: 10.1021/jp1115146.
- 62 L. Kou, C. Tang, Y. Zhang, T. Heine, C. Chen and T. Frauenheim, *J. Phys. Chem. Lett.*, 2012, **3**, 2934–2941.
- 63 Z. Wang, H. Li, Z. Liu, Z. Shi, J. Lu, K. Suenaga, S.-K. Joung, T. Okazaki, Z. Gu, J. Zhou, Z. Gao, G. Li, S. Sanvito, E. Wang and S. Iijima, *J. Am. Chem. Soc.*, 2010, **132**, 13840–13847, DOI: 10.1021/ja1058026.
- 64 E. Erdogan, I. H. Popov, A. N. Enyashin and G. Seifert, *Eur. Phys. J. B*, 2012, **85**, 33, DOI: 10.1140/epjb/e2011-20456-7.
- 65 H. Pan and Y.-W. Zhang, *J. Mater. Chem.*, 2012, **22**, 7280, DOI: 10.1039/c2jm15906f.
- 66 P. Lu, X. Wu, W. Guo and X. C. Zeng, *Phys. Chem. Chem. Phys.*, 2012, **14**, 13035, DOI: 10.1039/c2cp42181j.
- 67 K. Dolui, C. D. Pemmaraju and S. Sanvito, *ACS Nano*, 2012, **6**, 4823–4834, DOI: 10.1021/nn301505x.
- 68 Q. Yue, S. Chang, J. Kang, X. Zhang, Z. Shao, S. Qin and J. Li, *J. Phys.: Condens. Matter*, 2012, **24**, 335501, DOI: 10.1088/0953-8984/24/33/335501.
- 69 M. Sagynbaeva, P. Panigrahi, L. Yunguo, M. Ramzan and R. Ahuja, *Nanotechnology*, 2014, **25**, 165703, DOI: 10.1088/0957-4484/25/16/165703.
- 70 R.-L. Chu, G.-B. Liu, W. Yao, X. Xu, D. Xiao and C. Zhang, *Phys. Rev. B: Condens. Matter Mater. Phys.*, 2014, **89**, 155317, DOI: 10.1103/physrevb.89.155317.
- 71 C. Huang, S. Wu, A. M. Sanchez, J. J. P. Peters, R. Beanland, J. S. Ross, P. Rivera, W. Yao, D. H. Cobden and X. Xu, *Nat. Mater.*, 2014, **13**, 1096–1101, DOI: 10.1038/nmat4064.
- 72 A. Kormányos, V. Zólyomi, N. D. Drummond and G. Burkard, *Phys. Rev. X*, 2014, **4**, 011034, DOI: 10.1103/PhysRevX.4.011034.
- 73 G.-B. Liu, H. Pang, Y. Yao and W. Yao, *New J. Phys.*, 2014, **16**, 105011, DOI: 10.1088/1367-2630/16/10/105011.
- 74 H. L. Zhuang and R. G. Hennig, *J. Phys. Chem. C*, 2013, **117**, 20440–20445, DOI: 10.1021/jp405808a.
- 75 F. Besenbacher, M. Brorson, B. Clausen, S. Helveg, B. Hinnemann, J. Kibsgaard, J. Lauritsen, P. Moses, J. Nørskov and H. Topsøe, *Catal. Today*, 2008, **130**, 86–96, DOI: 10.1016/j.cattod.2007.08.009.
- 76 L. S. Byskov, J. K. Nørskov, B. S. Clausen and H. Topsøe, *J. Catal.*, 1999, **187**, 109–122, DOI: 10.1006/jcat.1999.2598.
- 77 J. Lauritsen, S. Helveg, E. Lægsgaard, I. Stensgaard, B. Clausen, H. Topsøe and F. Besenbacher, *J. Catal.*, 2001, **197**, 1–5, DOI: 10.1006/jcat.2000.3088.
- 78 J. Lauritsen, M. Bollinger, E. Lægsgaard, K. Jacobsen, J. Nørskov, B. Clausen, H. Topsøe and F. Besenbacher, *J. Catal.*, 2004, **221**, 510–522, DOI: 10.1016/j.jcat.2003.09.015.
- 79 J. Lauritsen, M. Nyberg, J. Nørskov, B. Clausen, H. Topsøe, E. Lægsgaard and F. Besenbacher, *J. Catal.*, 2004, **224**, 94–106, DOI: 10.1016/j.jcat.2004.02.009.
- 80 B. Hinnemann, P. G. Moses, J. Bonde, K. P. Jørgensen, J. H. Nielsen, S. Horch, I. Chorkendorff and J. K. Nørskov, *J. Am. Chem. Soc.*, 2005, **127**, 5308–5309, DOI: 10.1021/ja0504690.
- 81 T. F. Jaramillo, K. P. Jørgensen, J. Bonde, J. H. Nielsen, S. Horch and I. Chorkendorff, *Science*, 2007, **317**, 100–102, DOI: 10.1126/science.1141483.
- 82 J. Kibsgaard, Z. Chen, B. N. Reinecke and T. F. Jaramillo, *Nat. Mater.*, 2012, **11**, 963–969, DOI: 10.1038/nmat3439.
- 83 J. Kibsgaard, J. V. Lauritsen, E. Lægsgaard, B. S. Clausen, H. Topsøe and F. Besenbacher, *J. Am. Chem. Soc.*, 2006, **128**, 13950–13958, DOI: 10.1021/ja0651106.
- 84 A. Walton, J. Lauritsen, H. Topsøe and F. Besenbacher, *J. Catal.*, 2013, **308**, 306–318, DOI: 10.1016/j.jcat.2013.08.017.
- 85 R. Frindt, *J. Phys. Chem. Solids*, 1963, **24**, 1107–1112, DOI: 10.1016/0022-3697(63)90024-6.
- 86 R. F. Frindt and A. D. Yoffe, *Proc. R. Soc. A*, 1963, **273**, 69–83, DOI: 10.1098/rspa.1963.0075.
- 87 J. A. Wilson and A. D. Yoffe, *Adv. Phys.*, 1969, **18**, 193.
- 88 J. L. Verble and T. J. Wieting, *Phys. Rev. Lett.*, 1970, **25**, 362–365.
- 89 P. G. Harper and D. R. Edmodson, *Phys. Status Solidi B*, 1971, **44**, 59–69, DOI: 10.1002/pssb.2220440106.
- 90 R. A. Bromley, R. B. Murray and A. D. Yoffe, *J. Phys. C: Solid State Phys.*, 1972, **5**, 759.
- 91 B. Davey and B. L. Evans, *Phys. Status Solidi A*, 1972, **13**, 483–491.
- 92 D. R. Edmondson, *Solid State Commun.*, 1972, **10**, 1085–1088, DOI: 10.1016/0038-1098(72)90902-7.
- 93 L. Mattheiss, *Phys. Rev. Lett.*, 1973, **30**, 784–787, DOI: 10.1103/physrevlett.30.784.
- 94 L. F. Mattheiss, *Phys. Rev. B: Solid State*, 1973, **8**, 3719, DOI: 10.1103/PhysRevB.8.3719.
- 95 D. W. Bullett, *J. Phys. C: Solid State Phys.*, 1978, **11**, 4501.
- 96 X. Qian, J. Liu, L. Fu, J. Li, 2014, arXiv:1406.2749.
- 97 T. Jiang, H. Liu, D. Huang, S. Zhang, Y. Li, X. Gong, Y.-R. Shen, W.-T. Liu and S. Wu, *Nat. Nanotechnol.*, 2014, **9**, 825–829, DOI: 10.1038/nnano.2014.176.
- 98 R. Suzuki, M. Sakano, Y. J. Zhang, R. Akashi, D. Morikawa, A. Harasawa, K. Yaji, K. Kuroda, K. Miyamoto, T. Okuda,

- K. Ishizaka, R. Arita and Y. Iwasa, *Nat. Nanotechnol.*, 2014, **9**, 611–617, DOI: 10.1038/nnano.2014.148.
- 99 T. Böker, A. Müller, J. Augustin, C. Janowitz and R. Manzke, *Phys. Rev. B: Condens. Matter Mater. Phys.*, 1999, **60**, 4675.
- 100 G.-B. Liu, W.-Y. Shan, Y. Yao, W. Yao and D. Xiao, *Phys. Rev. B: Condens. Matter Mater. Phys.*, 2013, **88**, 085433, DOI: 10.1103/PhysRevB.88.085433.
- 101 D. Voß, P. Krüger, A. Mazur and J. Pollmann, *Phys. Rev. B: Condens. Matter Mater. Phys.*, 1999, **60**, 14311–14317, DOI: 10.1103/PhysRevB.60.14311.
- 102 T. Li and G. Galli, *J. Phys. Chem. C*, 2007, **111**, 16192–16196, DOI: 10.1021/jp075424v.
- 103 A. Klein, S. Tiefenbacher, V. Eyert, C. Pettenkofer and W. Jaegermann, *Thin Solid Films*, 2000, **380**, 221–223.
- 104 A. Klein, S. Tiefenbacher, V. Eyert, C. Pettenkofer and W. Jaegermann, *Phys. Rev. B: Condens. Matter Mater. Phys.*, 2001, **64**, 205416, DOI: 10.1103/PhysRevB.64.205416.
- 105 K. Albe and A. Klein, *Phys. Rev. B: Condens. Matter Mater. Phys.*, 2002, **66**, 073413, DOI: 10.1103/PhysRevB.66.073413.
- 106 Z. Y. Zhu, Y. C. Cheng and U. Schwingenschlögl, *Phys. Rev. B: Condens. Matter Mater. Phys.*, 2011, **84**, 153402, DOI: 10.1103/PhysRevB.84.153402.
- 107 H. Zeng, G.-B. Liu, J. Dai, Y. Yan, B. Zhu, R. He, L. Xie, S. Xu, X. Chen, W. Yao and X. Cui, *Sci. Rep.*, 2013, **3**, 1608, DOI: 10.1038/srep01608.
- 108 A. Ramasubramaniam, *Phys. Rev. B: Condens. Matter Mater. Phys.*, 2012, **86**, 115409, DOI: 10.1103/PhysRevB.86.115409.
- 109 H. Shi, H. Pan, Y.-W. Zhang and B. I. Yakobson, *Phys. Rev. B: Condens. Matter Mater. Phys.*, 2013, **87**, 155304, DOI: 10.1103/PhysRevB.87.155304.
- 110 J. Chang, L. F. Register and S. K. Banerjee, *J. Appl. Phys.*, 2014, **115**, 084506, DOI: 10.1063/1.4866872.
- 111 D. Wickramaratne, F. Zahid and R. K. Lake, *J. Chem. Phys.*, 2014, **140**, 124710, DOI: 10.1063/1.4869142.
- 112 W. Zhao, R. M. Ribeiro, M. Toh, A. Carvalho, C. Kloc, A. H. Castro Neto and G. Eda, *Nano Lett.*, 2013, **13**, 5627–5634, DOI: 10.1021/nl403270k.
- 113 L. Debbichi, O. Eriksson and S. Lebègue, *Phys. Rev. B: Condens. Matter Mater. Phys.*, 2014, **89**, 205311, DOI: 10.1103/physrevb.89.205311.
- 114 W. Feng, Y. Yao, W. Zhu, J. Zhou, W. Yao and D. Xiao, *Phys. Rev. B: Condens. Matter Mater. Phys.*, 2012, **86**, 165108, DOI: 10.1103/PhysRevB.86.165108.
- 115 K. Kośmider, J. W. González and J. Fernández-Rossier, *Phys. Rev. B: Condens. Matter Mater. Phys.*, 2013, **88**, 245436, DOI: 10.1103/PhysRevB.88.245436.
- 116 E. S. Kadantsev and P. Hawrylak, *Solid State Commun.*, 2012, **152**, 909–913, DOI: 10.1016/j.ssc.2012.02.005.
- 117 C.-H. Chang, X. Fan, S.-H. Lin and J.-L. Kuo, *Phys. Rev. B: Condens. Matter Mater. Phys.*, 2013, **88**, 195420, DOI: 10.1103/physrevb.88.195420.
- 118 E. Cappelluti, R. Roldán, J. A. Silva-Guillén, P. Ordejón and F. Guinea, *Phys. Rev. B: Condens. Matter Mater. Phys.*, 2013, **88**, 075409, DOI: 10.1103/PhysRevB.88.075409.
- 119 S. Horzum, H. Sahin, S. Cahangirov, P. Cudazzo, A. Rubio, T. Serin and F. M. Peeters, *Phys. Rev. B: Condens. Matter Mater. Phys.*, 2013, **87**, 125415, DOI: 10.1103/PhysRevB.87.125415.
- 120 M. Hybertsen and S. Louie, *Phys. Rev. Lett.*, 1985, **55**, 1418–1421, DOI: 10.1103/physrevlett.55.1418.
- 121 S. G. Louie and M. S. Hybertsen, *Int. J. Quantum Chem.*, 1987, **32**, 31–44, DOI: 10.1002/qua.560320706.
- 122 F. Aryasetiawan and O. Gunnarsson, *Rep. Prog. Phys.*, 1998, **61**, 237–312, DOI: 10.1088/0034-4885/61/3/002.
- 123 F. Hüser, T. Olsen and K. Thygesen, *Phys. Rev. B: Condens. Matter Mater. Phys.*, 2013, **88**, 245309, DOI: 10.1103/physrevb.88.245309.
- 124 Y. Liang, S. Huang, R. Soklaski and L. Yang, *Appl. Phys. Lett.*, 2013, **103**, 042106, DOI: 10.1063/1.4816517.
- 125 A. Kormányos, V. Zólyomi, N. D. Drummond, P. Rakytá, G. Burkard and V. I. Fal'ko, *Phys. Rev. B: Condens. Matter Mater. Phys.*, 2013, **88**, 045416, DOI: 10.1103/PhysRevB.88.045416.
- 126 G. Plechinger, F.-X. Schrettenbrunner, J. Eroms, D. Weiss, C. Schüller and T. Korn, *Phys. Status Solidi RRL*, 2012, **6**, 126–128, DOI: 10.1002/pssr.201105589.
- 127 B. K. Bußmann, K. Marinov, O. Ochedowski, N. Scheuschner, J. Maultzsch and M. Schleberger, *MRS Online Proc. Libr.*, 2012, **1474**, DOI: 10.1557/opl.2012.1463.
- 128 N. Scheuschner, O. Ochedowski, M. Schleberger and J. Maultzsch, *Phys. Status Solidi B*, 2012, **249**, 2644–2647, DOI: 10.1002/pssb.201200389.
- 129 H. J. Conley, B. Wang, J. I. Ziegler, R. F. Haglund, S. T. Pantelides and K. I. Bolotin, *Nano Lett.*, 2013, **13**, 3626–3630, DOI: 10.1021/nl4014748.
- 130 M. Buscema, G. A. Steele, H. S. J. van der Zant, A. Castellanos-Gómez, 2013, arXiv:1311.3869.
- 131 N. Scheuschner, O. Ochedowski, A.-M. Kaulitz, R. Gillen, M. Schleberger and J. Maultzsch, *Phys. Rev. B: Condens. Matter Mater. Phys.*, 2014, **89**, 125406, DOI: 10.1103/physrevb.89.125406.
- 132 M.-H. Chiu, C. Zhang, H. W. Shiu, C.-P. Chuu, C.-H. Chen, C.-Y. S. Chang, C.-H. Chen, M.-Y. Chou, C.-K. Shih, L.-J. Li, 2014, arXiv:1406.5137.
- 133 T. Cheiwchanwathanigij and W. R. L. Lambrecht, *Phys. Rev. B: Condens. Matter Mater. Phys.*, 2012, **85**, 205302, DOI: 10.1103/PhysRevB.85.205302.
- 134 H.-P. Komsa and A. V. Krasheninnikov, *Phys. Rev. B: Condens. Matter Mater. Phys.*, 2012, **86**, 241201(R), DOI: 10.1103/physrevb.86.241201.
- 135 T. C. Berkelbach, M. S. Hybertsen and D. R. Reichman, *Phys. Rev. B: Condens. Matter Mater. Phys.*, 2013, **88**, 045318, DOI: 10.1103/physrevb.88.045318.
- 136 E. Salpeter and H. Bethe, *Phys. Rev.*, 1951, **84**, 1232–1242, DOI: 10.1103/physrev.84.1232.
- 137 G. Onida and A. Rubio, *Rev. Mod. Phys.*, 2002, **74**, 601–659, DOI: 10.1103/revmodphys.74.601.
- 138 A. Molina-Sánchez, D. Sangalli, K. Hummer, A. Marini and L. Wirtz, *Phys. Rev. B: Condens. Matter Mater. Phys.*, 2013, **88**, 045412, DOI: 10.1103/PhysRevB.88.045412.
- 139 R. Soklaski, Y. Liang and L. Yang, *Appl. Phys. Lett.*, 2014, **104**, 193110, DOI: 10.1063/1.4878098.

- 140 H. Yu, G.-B. Liu, P. Gong, X. Xu and W. Yao, *Nat. Commun.*, 2014, **5**, 3876, DOI: 10.1038/ncomms4876.
- 141 K. Kośmider and J. Fernández-Rossier, *Phys. Rev. B: Condens. Matter Mater. Phys.*, 2013, **87**, 075451, DOI: 10.1103/PhysRevB.87.075451.
- 142 R. Roldán, M. P. López-Sancho, E. Cappelluti, J. A. Silva-Guillén, P. Ordejón, F. Guinea, 2014, arXiv:1401.5009.
- 143 T. Cheiwchanwathanangij, W. R. L. Lambrecht, Y. Song and H. Dery, *Phys. Rev. B: Condens. Matter Mater. Phys.*, 2013, **88**, 155404, DOI: 10.1103/PhysRevB.88.155404.
- 144 H. Ochoa and R. Roldán, *Phys. Rev. B: Condens. Matter Mater. Phys.*, 2013, **87**, 245421, DOI: 10.1103/physrevb.87.245421.
- 145 P. Rivera, J. R. Schaibley, A. M. Jones, J. S. Ross, S. Wu, G. Aivazian, P. Klement, N. J. Ghimire, J. Yan, D. G. Mandrus, W. Yao, X. Xu, 2014, arXiv:1403.4985.
- 146 D. Xiao, M.-C. Chang and Q. Niu, *Rev. Mod. Phys.*, 2010, **82**, 1959–2007, DOI: 10.1103/RevModPhys.82.1959.
- 147 W. S. Yun, S. W. Han, S. C. Hong, I. G. Kim and J. D. Lee, *Phys. Rev. B: Condens. Matter Mater. Phys.*, 2012, **85**, 033305, DOI: 10.1103/PhysRevB.85.033305.
- 148 T. Li, *Phys. Rev. B: Condens. Matter Mater. Phys.*, 2012, **85**, 235407, DOI: 10.1103/physrevb.85.235407.
- 149 P. Johari and V. B. Shenoy, *ACS Nano*, 2012, **6**, 5449–5456, DOI: 10.1021/nn301320r.
- 150 Q. Yue, J. Kang, Z. Shao, X. Zhang, S. Chang, G. Wang, S. Qin and J. Li, *Phys. Lett. A*, 2012, **376**, 1166–1170, DOI: 10.1016/j.physleta.2012.02.029.
- 151 E. Scalise, M. Houssa, G. Pourtois, V. Afanas'ev and A. Stesmans, *Nano Res.*, 2012, **5**, 43–48, DOI: 10.1007/s12274-011-0183-0.
- 152 C. Rice, R. Young, R. Zan, U. Bangert, D. Wolverson, T. Georgiou, R. Jalil and K. Novoselov, *Phys. Rev. B: Condens. Matter Mater. Phys.*, 2013, **87**, 081307, DOI: 10.1103/physrevb.87.081307.
- 153 Q. Zhang, Y. Cheng, L.-Y. Gan and U. Schwingenschlögl, *Phys. Rev. B: Condens. Matter Mater. Phys.*, 2013, **88**, 245447, DOI: 10.1103/physrevb.88.245447.
- 154 M. A. Cazalilla, H. Ochoa, F. Guinea, 2013, arXiv:1311.6650.
- 155 J. Qi, X. Li, X. Chen and K. Hu, *J. Phys.: Condens. Matter*, 2014, **26**, 256003, DOI: 10.1088/0953-8984/26/25/256003.
- 156 E. Scalise, M. Houssa, G. Pourtois, V. Afanas'ev and A. Stesmans, *Phys. E*, 2014, **56**, 416–421, DOI: 10.1016/j.physe.2012.07.029.
- 157 Y. Ge, W. Wan, W. Feng, D. Xiao and Y. Yao, *Phys. Rev. B: Condens. Matter Mater. Phys.*, 2014, **90**, 035414, DOI: 10.1103/physrevb.90.035414.
- 158 C. R. Zhu, G. Wang, B. L. Liu, X. Marie, X. F. Qiao, X. Zhang, X. X. Wu, H. Fan, P. H. Tan, T. Amand and B. Urbaszek, *Phys. Rev. B: Condens. Matter Mater. Phys.*, 2013, **88**, 121301(R), DOI: 10.1103/physrevb.88.121301.
- 159 K. He, C. Poole, K. F. Mak and J. Shan, *Nano Lett.*, 2013, **13**, 2931–2936, DOI: 10.1021/nl4013166.
- 160 A. Castellanos-Gómez, R. Roldán, E. Cappelluti, M. Buscema, F. Guinea, H. S. J. van der Zant and G. A. Steele, *Nano Lett.*, 2013, **13**, 5361–5366, DOI: 10.1021/nl402875m.
- 161 F. Guinea, B. Horovitz and P. Le Doussal, *Phys. Rev. B: Condens. Matter Mater. Phys.*, 2008, **77**, 205421, DOI: 10.1103/PhysRevB.77.205421.
- 162 N. Levy, S. A. Burke, K. L. Meaker, M. Panlasigui, A. Zettl, F. Guinea, A. H. C. Neto and M. F. Crommie, *Science*, 2010, **329**, 544–547, DOI: 10.1126/science.1191700.
- 163 M. Vozmediano, M. Katsnelson and F. Guinea, *Phys. Rep.*, 2010, **496**, 109–148, DOI: 10.1016/j.physrep.2010.07.003.
- 164 M. A. Cazalilla, H. Ochoa and F. Guinea, *Phys. Rev. Lett.*, 2014, **113**, 077201, DOI: 10.1103/physrevlett.113.077201.
- 165 S. Bhattacharyya and A. K. Singh, *Phys. Rev. B: Condens. Matter Mater. Phys.*, 2012, **86**, 075454, DOI: 10.1103/PhysRevB.86.075454.
- 166 Q. Liu, L. Li, Y. Li, Z. Gao, Z. Chen and J. Lu, *J. Phys. Chem. C*, 2012, **116**, 21556–21562, DOI: 10.1021/jp307124d.
- 167 J. He, K. Hummer and C. Franchini, *Phys. Rev. B: Condens. Matter Mater. Phys.*, 2014, **89**, 075409, DOI: 10.1103/physrevb.89.075409.
- 168 A. Kuc, N. Zibouche and T. Heine, *Phys. Rev. B: Condens. Matter Mater. Phys.*, 2011, **83**, 245213, DOI: 10.1103/physrevb.83.245213.
- 169 J. K. Ellis, M. J. Lucero and G. E. Scuseria, *Appl. Phys. Lett.*, 2011, **99**, 261908, DOI: 10.1063/1.3672219.
- 170 A. Ramasubramaniam, D. Naveh and E. Towe, *Phys. Rev. B: Condens. Matter Mater. Phys.*, 2011, **84**, 205325, DOI: 10.1103/PhysRevB.84.205325.
- 171 A. Kumar and P. K. Ahluwalia, *Eur. Phys. J. B*, 2012, **85**, 186, DOI: 10.1140/epjb/e2012-30070-x.
- 172 S. W. Han, H. Kwon, S. K. Kim, S. Ryu, W. S. Yun, D. H. Kim, J. H. Hwang, J.-S. Kang, J. Baik, H. J. Shin and S. C. Hong, *Phys. Rev. B: Condens. Matter Mater. Phys.*, 2011, **84**, 045409, DOI: 10.1103/physrevb.84.045409.
- 173 F. Zahid, L. Liu, Y. Zhu, J. Wang and H. Guo, *AIP Adv.*, 2013, **3**, 052111, DOI: 10.1063/1.4804936.
- 174 S. Grimme, *J. Comput. Chem.*, 2006, **27**, 1787–1799, DOI: 10.1002/jcc.20495.
- 175 W. Jin, P.-C. Yeh, N. Zaki, D. Zhang, J. T. Sadowski, A. Al-Mahboob, A. M. van der Zande, D. A. Chenet, J. I. Dadap, I. P. Herman, P. Sutter, J. Hone and R. M. Osgood, *Phys. Rev. Lett.*, 2013, **111**, 106801, DOI: 10.1103/PhysRevLett.111.106801.
- 176 N. Zibouche, P. Philipsen, A. Kuc, T. Heine, 2014, arXiv:1406.5012.
- 177 H. Yuan, M. S. Bahramy, K. Morimoto, S. Wu, K. Nomura, B.-J. Yang, H. Shimotani, R. Suzuki, M. Toh, C. Kloc, X. Xu, R. Arita, N. Nagaosa and Y. Iwasa, *Nat. Phys.*, 2013, **9**, 563–569, DOI: 10.1038/nphys2691.
- 178 C.-H. Lee, G.-H. Lee, A. M. van der Zande, W. Chen, Y. Li, M. Han, X. Cui, G. Arefe, C. Nuckolls, T. F. Heinz, J. Guo, J. Hone, P. Kim, 2014, arXiv:1403.3062.
- 179 M. M. Furchi, A. Pospischil, F. Libisch, J. Burgdörfer, T. Mueller, 2014, arXiv:1403.2652.
- 180 R. Cheng, D. Li, H. Zhou, C. Wang, A. Yin, S. Jiang, Y. Liu, Y. Chen, Y. Huang, X. Duan, 2014, arXiv:1403.3447.
- 181 H. Fang, C. Battaglia, C. Carraro, S. Nemsak, B. Ozdol, J. S. Kang, H. A. Bechtel, S. B. Desai, F. Kronast, A. A. Unal,

- G. Conti, C. Conlon, G. K. Palsson, M. C. Martin, A. M. Minor, C. S. Fadley, E. Yablonovitch, R. Maboudian, A. Javey, 2014, arXiv:1403.3754.
- 182 L. Britnell, R. M. Ribeiro, A. Eckmann, R. Jalil, B. D. Belle, A. Mishchenko, Y.-J. Kim, R. V. Gorbachev, T. Georgiou, S. V. Morozov, A. N. Grigorenko, A. K. Geim, C. Casiraghi, A. H. Castro Neto and K. S. Novoselov, *Science*, 2013, **340**, 1311–1314, DOI: 10.1126/science.1235547.
- 183 H. Terrones, F. López-Urías and M. Terrones, *Sci. Rep.*, 2013, **3**, 1549, DOI: 10.1038/srep01549.
- 184 N. Lu, H. Guo, L. Li, J. Dai, L. Wang, W.-N. Mei, X. Wu and X. C. Zeng, *Nanoscale*, 2014, **6**, 2879, DOI: 10.1039/c3nr06072a.
- 185 H.-P. Komsa and A. V. Krasheninnikov, *Phys. Rev. B: Condens. Matter Mater. Phys.*, 2013, **88**, 085318, DOI: 10.1103/PhysRevB.88.085318.
- 186 H. Mirhosseini, G. Roma, J. Kiss and C. Felser, *Phys. Rev. B: Condens. Matter Mater. Phys.*, 2014, **89**, 205301, DOI: 10.1103/physrevb.89.205301.
- 187 J. Kang, J. Li, S.-S. Li, J.-B. Xia and L.-W. Wang, *Nano Lett.*, 2013, **13**, 5485–5490, DOI: 10.1021/nl4030648.
- 188 R. Coehoorn, C. Haas, J. Dijkstra, C. J. F. Flipse, R. A. de Groot and A. Wold, *Phys. Rev. B: Condens. Matter Mater. Phys.*, 1987, **35**, 6195–6202, DOI: 10.1103/physrevb.35.6195.
- 189 W. Schutte, J. De Boer and F. Jellinek, *J. Solid State Chem.*, 1987, **70**, 207–209, DOI: 10.1016/0022-4596(87)90057-0.
- 190 M. M. Fogler, L. V. Butov, K. S. Novoselov, 2014, arXiv: 1404.1418.
- 191 H. Rostami, A. G. Moghaddam and R. Asgari, *Phys. Rev. B: Condens. Matter Mater. Phys.*, 2013, **88**, 085440, DOI: 10.1103/PhysRevB.88.085440.
- 192 F. Rose, M. O. Goerbiger and F. Piéchon, *Phys. Rev. B: Condens. Matter Mater. Phys.*, 2013, **88**, 125438, DOI: 10.1103/PhysRevB.88.125438.
- 193 X. Li, F. Zhang and Q. Niu, *Phys. Rev. Lett.*, 2013, **110**, 066803, DOI: 10.1103/PhysRevLett.110.066803.
- 194 H.-Z. Lu, W. Yao, D. Xiao and S.-Q. Shen, *Phys. Rev. Lett.*, 2013, **110**, 016806, DOI: 10.1103/PhysRevLett.110.016806.
- 195 F. Parhizgar, H. Rostami and R. Asgari, *Phys. Rev. B: Condens. Matter Mater. Phys.*, 2013, **87**, 125401, DOI: 10.1103/PhysRevB.87.125401.
- 196 Z. Li and J. P. Carbotte, *Phys. Rev. B: Condens. Matter Mater. Phys.*, 2012, **86**, 205425, DOI: 10.1103/PhysRevB.86.205425.
- 197 J. Klinovaja and D. Loss, *Phys. Rev. B: Condens. Matter Mater. Phys.*, 2013, **88**, 075404, DOI: 10.1103/physrevb.88.075404.
- 198 Z. Li and J. Carbotte, *Phys. B*, 2013, **421**, 97–104, DOI: 10.1016/j.physb.2013.04.030.
- 199 T. Cai, S. A. Yang, X. Li, F. Zhang, J. Shi, W. Yao and Q. Niu, *Phys. Rev. B: Condens. Matter Mater. Phys.*, 2013, **88**, 115140, DOI: 10.1103/PhysRevB.88.115140.
- 200 W.-Y. Shan, H.-Z. Lu and D. Xiao, *Phys. Rev. B: Condens. Matter Mater. Phys.*, 2013, **88**, 125301, DOI: 10.1103/physrevb.88.125301.
- 201 C. Zhang, H. Wang, W. Chan, C. Manolatou and F. Rana, *Phys. Rev. B: Condens. Matter Mater. Phys.*, 2014, **89**, 205435, DOI: 10.1103/physrevb.89.205436.
- 202 T. Yu and M. W. Wu, *Phys. Rev. B: Condens. Matter Mater. Phys.*, 2014, **89**, 205303, DOI: 10.1103/physrevb.89.205303.
- 203 Y. C. Cheng, Q. Y. Zhang and U. Schwingenschlögl, *Phys. Rev. B: Condens. Matter Mater. Phys.*, 2014, **89**, 155429, DOI: 10.1103/physrevb.89.155429.
- 204 J. F. Sun and F. Cheng, *J. Appl. Phys.*, 2014, **115**, 133703, DOI: 10.1063/1.4870290.
- 205 A. S. Rodin and A. H. Castro Neto, *Phys. Rev. B: Condens. Matter Mater. Phys.*, 2013, **88**, 195437, DOI: 10.1103/physrevb.88.195437.
- 206 T. Stroucken, S. W. Koch, 2014, arXiv:1404.4238.
- 207 H. Rostami and R. Asgari, *Phys. Rev. B: Condens. Matter Mater. Phys.*, 2014, **89**, 115413, DOI: 10.1103/physrevb.89.115413.
- 208 A. Scholz, T. Stauber and J. Schliemann, *Phys. Rev. B: Condens. Matter Mater. Phys.*, 2013, **88**, 035135, DOI: 10.1103/physrevb.88.035135.
- 209 L. Wang and M. W. Wu, *Phys. Rev. B: Condens. Matter Mater. Phys.*, 2014, **89**, 115302, DOI: 10.1103/physrevb.89.115302.
- 210 J. C. Slater and G. F. Koster, *Phys. Rev.*, 1954, **94**, 1498–1524, DOI: 10.1103/PhysRev.94.1498.
- 211 P.-O. Löwdin, *J. Chem. Phys.*, 1951, **19**, 1396, DOI: 10.1063/1.1748067.
- 212 R. Winkler, *Spin-orbit Coupling Effects in Two-Dimensional Electron and Hole Systems*, Springer, Berlin, 2003, vol. 191.
- 213 Y.-H. Ho, Y.-H. Wang and H.-Y. Chen, *Phys. Rev. B: Condens. Matter Mater. Phys.*, 2014, **89**, 155316, DOI: 10.1103/physrevb.89.155316.
- 214 R.-L. Chu, X. Li, S. Wu, Q. Niu, W. Yao, X. Xu and C. Zhang, *Phys. Rev. B: Condens. Matter Mater. Phys.*, 2014, **90**, 045427, DOI: 10.1103/PhysRevB.90.045427.
- 215 J. T. Ye, Y. J. Zhang, R. Akashi, M. S. Bahramy, R. Arita and Y. Iwasa, *Science*, 2012, **338**, 1193–1196, DOI: 10.1126/science.1228006.